

# Classification of radio backgrounds at cosmic dawn and 21-cm signal confirmation using neural networks

Sudipta Sikder,<sup>1</sup>★ Anastasia Fialkov<sup>2,3</sup> and Rennan Barkana<sup>1</sup>

<sup>1</sup>*School of Physics and Astronomy, Tel-Aviv University, Tel-Aviv, 69978, Israel*

<sup>2</sup>*Institute of Astronomy, University of Cambridge, Madingley Road, Cambridge, CB3 0HA, UK*

<sup>3</sup>*Kavli Institute for Cosmology, Madingley Road, Cambridge, CB3 0HA, UK*

Accepted XXX. Received YYY; in original form ZZZ

## ABSTRACT

Several ongoing and upcoming radio telescopes aim to detect either the global 21-cm signal or the 21-cm power spectrum. The extragalactic radio background, as detected by ARCADE-2 and LWA-1, suggests a strong radio background from cosmic dawn, which can significantly alter the cosmological 21-cm signal, enhancing both the global signal amplitude and the 21-cm power spectrum. In this paper, we employ an artificial neural network (ANN) to check if there is a radio excess over the Cosmic Microwave Background (CMB) in mock data, and if present, we classify its type into one of two categories, a background from high-redshift radio galaxies or a uniform exotic background from the early Universe. Based on clean data (without observational noise), the ANN can predict the background radiation type with 96% accuracy for the power spectrum and 90% for the global signal. Although observational noise reduces the accuracy, the results remain quite useful. We also apply ANNs to map the relation between the 21-cm power spectrum and the global signal. By reconstructing the global signal using the 21-cm power spectrum, an ANN can estimate the global signal range consistent with an observed power spectrum from SKA-like experiments. Conversely, we show that an ANN can reconstruct the 21-cm power spectrum over a wide range of redshifts and wavenumbers given the global signal over the same redshifts. Such trained networks can potentially serve as a valuable tool for cross-confirmation of the 21-cm signal.

**Key words:** methods: numerical – methods: statistical – dark ages, reionization, first stars – cosmology: theory

## 1 INTRODUCTION

The 21-cm signal produced by neutral hydrogen atoms in the intergalactic medium is one of the most promising probes of the Epoch of Reionization (EoR) and cosmic dawn. Due to the expansion of the universe, this signal is redshifted to frequencies below 200 MHz and, therefore, is expected to be observed by low-frequency radio telescopes. The Experiment to Detect the Global EoR Signature (EDGES) reported the first tentative detection of the sky-averaged (global) 21-cm signal from  $z \sim 17$  using the low band antenna in the 50 – 200 MHz frequency range (Bowman et al. 2018). However, the SARAS3 experiment (Singh et al. 2022) reported an upper limit of the global 21-cm signal which is inconsistent at  $2\sigma$  with the EDGES signal. Other ongoing global experiments such as Sonda Cosmológica de las Islas para la Detección de Hidrógeno Neutro (SCI-HI, Voytek et al. 2014), Probing Radio Intensity at high-Z (PRIZM, Philip et al. 2019), Mapper of the IGM Spin Temperature (MIST, Monsalve et al. 2024), Radio Experiment for the Analysis of Cosmic Hydrogen (REACH, de Lera Acedo et al. 2022) may soon validate or refute the purported EDGES claims. On another front, several observational efforts have been made to try to measure the spatial fluctuations in the 21-cm signal, i.e., the 21-cm power spectrum from the EoR and cosmic dawn. These used radio interfer-

ometers including the Low Frequency Array (LOFAR, Gehlot et al. 2019), the Murchison Wide-field Array (MWA, Trott et al. 2020), the Owens Valley Radio Observatory Long Wavelength Array (OVRO-LWA, Eastwood et al. 2019), the Large-aperture Experiment to detect the Dark Age (LEDA, Price et al. 2018; Garsden et al. 2021), the New Extension in Nançay Upgrading LOFAR (NenuFAR, Mertens et al. 2021), and the Hydrogen Epoch of Reionization Array (HERA, DeBoer et al. 2017; Abdurashidova et al. 2022b). The upcoming Square Kilometre Array (SKA, Koopmans et al. 2015) is expected to provide measurements of the 21-cm power spectrum over a wide range of redshifts including cosmic dawn.

Although semi-numerical simulations (Mesinger et al. 2011; Visbal et al. 2012; Fialkov & Barkana 2014; Cohen et al. 2017) are significantly faster than full cosmological hydrodynamical simulations, each run can still take hours to calculate the 21-cm signal from a wide range of redshifts and large cosmological volume. To accurately constrain astrophysical parameters, using semi-numerical simulations directly is computationally demanding. Instead, emulators trained using an Artificial Neural Network (ANN) can be utilized to generate the desired statistical description of the signal in a fraction of a second. Such emulation methods drastically speed up the parameter explorations of astrophysical processes using observational data. Various works have been done on the emulation of the global 21-cm signal and the 21-cm power spectrum. The first global signal emulator based on ANN was introduced by Cohen et al. (2020).

★ E-mail: sudiptas@mail.tau.ac.il

Recently, different approaches based on ANN have been proposed to emulate the global signal more accurately (Bevins et al. 2021; Bye et al. 2022). Kern et al. (2017) proposed a fast emulator for the 21-cm power spectrum and performed Bayesian analysis to constrain an eleven parameter model that included six parameters of reionization and X-ray heating and five additional cosmological parameters. Schmit & Pritchard (2018) used an ANN to emulate the 21-cm power spectrum and compared their analysis to constraining three EoR parameters with 21CMMC (Greig & Mesinger 2015). Some of these emulators have been used to find constraints on astrophysical parameters (Mondal et al. 2020; Abdurashidova et al. 2022a; HERA Collaboration et al. 2023; Bevins et al. 2022, 2024). In our previous work (Sikder et al. 2024a), we constructed an ANN-based emulation method to constrain uncertainties in a seven-parameter astrophysical model using a mock SKA dataset of the 21-cm power spectrum, where we added the expected SKA noise and other observational effects to the simulated power spectrum. In addition, we considered astrophysical models with two types of excess radio backgrounds: external radio background models, which refer to a homogeneous radio background with a redshift-independent amplitude that is not directly associated with astrophysical sources, as proposed by Fialkov & Barkana (2019); and galactic radio models, which refer to excess radio emission from high redshift galaxies, as suggested by Reis et al. (2020). We built an ANN to infer the type of radio background present in the 21-cm power spectrum. However, we did not compare with models with a standard astrophysical scenario (where the Cosmic Microwave Background (CMB) is the only source of background radio emission) in the classification procedure. In this work, we construct an ANN classifier and apply the trained classifier on a dataset of three different radio background models in order to identify the type of radio background in the 21-cm signal from cosmic dawn and the EoR. We show for the first time that the global 21-cm signal as well as the power spectrum over a wide range of redshifts can be used to infer the presence and type of radio background present in the signal using an ANN based classifier.

Although fast progress in observational 21-cm cosmology is being made, we do not yet know whether the global signal or the power spectrum will be measured more precisely in the near future. So in the current early state of observations, an interesting theoretical question arises as to how well we can determine the global 21-cm signal given a measurement of the power spectrum from observations like the SKA. We address this question in the second part of this work. We present an ANN to predict the global 21-cm signal from cosmic dawn and the EoR given the 21-cm power spectrum over the same redshifts. This method could, in principle, test whether or not independent observations by radiometers and interferometers are consistent. We also consider the inverse direction. With the type of radio background successfully established from a global signal measurement using our classification method described in the previous paragraph, we show that another ANN can be used to reconstruct the power spectrum. Using this trained network, we could potentially put constraints on the 21-cm power spectrum from an observed global signal. Such methods could be used to test the consistency between future detections of the global signal and power spectrum, and thus are useful for the purpose of verification of the 21-cm signal.

This paper is organized as follows: In Section 2, we describe the theoretical background of the astrophysics of the high redshift Universe and the 21-cm signal. We discuss the method to generate the datasets and the details of the neural network architecture in Section 3. Sections 4 and 5 present the results of this work. Finally, we conclude in Section 6.

## 2 THEORETICAL BACKGROUND

### 2.1 Astrophysics at high redshift

We use our simulation code 21-cm Semi-numerical Predictions Across Cosmological Epochs (21cmSPACE, Visbal et al. 2012; Fialkov & Barkana 2014, 2019; Cohen et al. 2017). We simulate realizations of the universe in a  $(384 \text{ Mpc})^3$  comoving cosmological volume over the redshift range 6 – 35 thus including cosmic dawn and reionization. Following hierarchical structure formation, the simulation keeps track of star formation, evolution of the X-ray and Ly- $\alpha$  backgrounds, and other radiative feedback mechanisms (such as the effect of Lyman-Werner feedback and photoheating feedback on star formation). We parameterize the high redshift universe using eight key parameters which regulate several astrophysical processes including star formation, heating, ionization, and an excess radio background.

Given the power spectra of initial density and velocity fields (calculated using the publicly available code CAMB, Lewis et al. 2000), a random realization of the linear density field and relative velocity field between dark matter and baryons (Tsaliakhovich & Hirata 2010) are calculated on a  $128^3$  grid with a resolution (pixel size) of 3 comoving Mpc. The density and velocity fields are then evolved linearly. We obtain the population of collapsed dark matter halos in each cell at each redshift using a modified Press-Schechter model (Press & Schechter 1974; Sheth & Tormen 1999; Barkana & Loeb 2004). The dark matter halo population that can form stars is determined by the minimum circular velocity ( $V_c$ ) of the halos, a free parameter in the simulation. Another free parameter encoding the information about star formation is the fractional amount of gas in star-forming halos that is converted into stars, referred to as the star formation efficiency ( $f_\star$ ). The simulation takes into account the suppression of star formation due to the above-mentioned relative velocity between dark matter and baryons, Lyman-Werner feedback (Haiman et al. 1997; Fialkov et al. 2013), photoheating feedback during the EoR (Rees 1986; Sobacchi & Mesinger 2013; Cohen et al. 2016), and also Ly- $\alpha$  and CMB heating (Reis et al. 2021).

Given a galaxy population, the simulation calculates radiation fields emitted by those galaxies. The intensity of the Ly- $\alpha$  radiation is calculated assuming that galaxies contain population II stars. The dominant contribution to the X-ray luminosity ( $L_X$ ) in galaxies is likely to be from X-ray binaries. To parameterize the total X-ray luminosity of various sources, galactic halos are assumed to have an X-ray luminosity that scales with the star formation rate (e.g., Grimm et al. 2003; Gilfanov et al. 2004; Mineo et al. 2012; Fragos et al. 2013; Fialkov et al. 2014; Pacucci et al. 2014). The scaling is such that the standard normalization factor (which we denote as an X-ray radiation efficiency  $f_X = 1$ ) corresponds to the X-ray luminosity of present day low-metallicity galaxies. As  $f_X$  has relatively weak observational constraints at the relevant redshifts (Fialkov et al. 2017; Abdurashidova et al. 2022a; Bevins et al. 2024), we vary  $f_X$  from 0.0001 to 1000. In addition to the X-ray efficiency  $f_X$ , the SED of the X-ray sources is another key astrophysical parameter. We assume that the X-ray SED has a power law shape with a slope  $\alpha$  and low energy cutoff  $E_{\min}$ . We vary  $\alpha$  in the range 1 – 1.5 and  $E_{\min}$  in the range 0.1 – 3.0 keV.

The process of reionization is parameterized with two parameters: one is the ionizing efficiency  $\zeta$  of sources. Given that, for a specific choice of other astrophysical parameters, there exists a one-to-one relationship between the CMB optical depth ( $\tau$ ) and the ionizing efficiency ( $\zeta$ ), and as  $\tau$  is directly probed by CMB observations (Planck Collaboration et al. 2020), we opt to incorporate  $\tau$  as part of our astrophysical model instead of the ionizing efficiency ( $\zeta$ ). Another EoR parameter is the mean free path of the ionizing photons,

$R_{\text{mfp}}$ , which we vary between 10 and 70 comoving Mpc (Wyithe & Loeb 2004; Songaila & Cowie 2010). This parameter quantifies the maximum possible radius of an ionized bubble during the EoR, and is important only in the latter stages.

The above describes our standard astrophysics model. The simulation also includes the possibility of an excess radio background over the CMB. This feature is discussed in detail in Section 2.3.

## 2.2 21-cm signal

The 21-cm brightness temperature  $T_{21}$  measures the 21-cm intensity on the sky. In the low optical depth regime (where the 21-cm optical depth,  $\tau_{21} \ll 1$ ), the 21-cm brightness temperature can be approximated as

$$T_{21} \approx 26.8 \left( \frac{\Omega_b h}{0.0327} \right) \left( \frac{\Omega_m}{0.307} \right)^{-1/2} \left( \frac{1+z}{10} \right)^{1/2} (1+\delta) x_{\text{HI}} \frac{x_{\text{tot}}}{1+x_{\text{tot}}} \left( 1 - \frac{T_{\text{rad}}}{T_{\text{K}}} \right) \text{ mK}, \quad (1)$$

where  $\delta$  is the density contrast,  $x_{\text{HI}}$  is the neutral hydrogen fraction, and the coupling coefficient  $x_{\text{tot}}$  is the sum of the contributions of the Ly- $\alpha$  coupling ( $x_\alpha$ ) and the collisional coupling ( $x_c$ ), i.e.,  $x_{\text{tot}} = x_\alpha + x_c$ . The standard astrophysical scenario assumes the background radiation to be the CMB, in which case  $T_{\text{rad}} = T_{\text{CMB}} = 2.725(1+z)$  K. In the presence of an excess radio background of brightness temperature  $T_{\text{Radio}}$ , the total radio background can be written as

$$T_{\text{rad}} = T_{\text{CMB}} + T_{\text{Radio}}. \quad (2)$$

There are two approaches to measuring the 21-cm signal. The first is to integrate over a large area on the sky with a single antenna and find the sky-averaged (global) spectrum, which tracks the evolution of the signal with time/redshift. The second approach is to use interferometry and measure the evolution of the fluctuations in the 21-cm signal. This yields a much richer dataset that gives spatial information over a wide range of wavenumbers at each redshift. The 21-cm power spectrum of the brightness temperature fluctuations is defined as

$$\langle \tilde{\delta}_{T_b}(\mathbf{k}) \tilde{\delta}_{T_b}^*(\mathbf{k}') \rangle = (2\pi)^3 \delta_D(\mathbf{k} - \mathbf{k}') P(\mathbf{k}), \quad (3)$$

where  $\mathbf{k}$  is the comoving wave vector,  $\delta_D$  is the Dirac delta function,  $\tilde{\delta}_{T_b}(\mathbf{k})$  is the Fourier transform of  $\delta_{T_b}(\mathbf{x})$  which is defined by  $\delta_{T_b}(\mathbf{x}) = (T_{21}(\mathbf{x}) - \langle T_{21} \rangle) / \langle T_{21} \rangle$ , and the angular brackets denote the ensemble or spatial average. It is conventional to express the power spectrum in terms of the variance in  $\text{mK}^2$  units as follows:

$$\Delta^2 = \langle T_{21} \rangle^2 \frac{k^3 P(k)}{2\pi^2}. \quad (4)$$

Although the 21-cm power spectrum does not capture all the available statistical information, due to the non-Gaussian fluctuations sourced by non-linear processes over both large and small scales during cosmic dawn and the EoR, it remains an invaluable tool to reveal significant astrophysical insights. Its measurement is relatively straightforward through observations compared to higher order statistics such as the 21-cm bispectrum (Lewis 2011; Majumdar et al. 2018), trispectrum (Cooray et al. 2008), etc.

## 2.3 Excess radio background models

As mentioned in the introduction, though not yet independently confirmed, a possible detection of the 21-cm signal from cosmic dawn

( $z \sim 17$ ) has been claimed by the EDGES collaboration (Bowman et al. 2018). The reported signal has an absorption trough which is a factor of two larger in amplitude than what is predicted by a standard astrophysical model based on the  $\Lambda$ CDM cosmology and hierarchical structure formation (Cohen et al. 2017; Reis et al. 2021). This unexpectedly strong absorption signature, if it is cosmological (rather than instrumental or due to foregrounds), signifies a large difference between the spin temperature of neutral hydrogen and the temperature of the radiation background. A modification of the standard astrophysical model is required to explain the anomalous absorption signal. Barkana (2018) showed that interaction of cold dark matter with the cosmic gas could introduce an additional cooling mechanism, making the neutral hydrogen gas colder than expected (see also Berlin et al. 2018; Barkana et al. 2018a; Muñoz & Loeb 2018; Liu et al. 2019; Cheung et al. 2019; Barkana et al. 2018b, 2023; Kovetz et al. 2018). Another potential explanation involves the presence of an excess radio background over the CMB (Bowman et al. 2018; Feng & Holder 2018; Ewall-Wice et al. 2018; Fialkov & Barkana 2019; Mirocha & Furlanetto 2019; Ewall-Wice et al. 2020; Reis et al. 2020). In this paper we focus on the second explanation and explore two different types of excess radio background models<sup>1</sup>.

• **External radio background:** Fialkov & Barkana (2019) proposed that the EDGES detection, if confirmed, can be explained by an excess homogeneous radio background with a redshift-independent amplitude and synchrotron-like spectrum in the early Universe. This background would not be directly related to astrophysical sources and could instead be generated by exotic processes such as dark matter decay. The total radio background due to this phenomenological uniform excess, with a form that is inspired by ARCADE2 (Fixsen et al. 2011; Seiffert et al. 2011) and LWA1 (Dowell & Taylor 2018) observations, can be written as

$$T_{\text{rad}} = T_{\text{CMB}} (1+z) \left[ 1 + A_r \left( \frac{\nu_{\text{obs}}}{78 \text{ MHz}} \right)^\beta \right] \text{ K}, \quad (5)$$

where  $T_{\text{CMB}}$  is the CMB temperature today,  $\nu_{\text{obs}}$  is the observed frequency, the spectral index  $\beta = -2.6$  and the constant  $A_r$  is the amplitude of this uniform radio background relative to the CMB. Thus, in total, we have eight free parameters for the external radio model:  $f_\star$ ,  $V_c$ ,  $f_X$ ,  $\alpha$ ,  $E_{\text{min}}$ ,  $\tau$ ,  $R_{\text{mfp}}$  and  $A_r$ .

• **Galactic radio background:** In contrast with the phenomenological external radio model, a fluctuating radio excess could originate from astrophysical sources such as active galactic nuclei (AGN, Urry & Padovani 1995; Biermann et al. 2014; Bolgar et al. 2018; Ewall-Wice et al. 2018, 2020) or star-forming galaxies (Condon 1992; Jana et al. 2019) at high redshift. The effect of this inhomogeneous excess galactic radio background on the global 21-cm signal and the 21-cm power spectrum was explored by Reis et al. (2020) who first incorporated it into semi-numerical simulations of the early Universe. Here we use those models (but note that in our recent work (Sikder et al. 2024b), we presented an improved modelling of the non-uniform radio fluctuations, incorporating a line-of-sight effect). The modelling of this galactic radio background assumes the galaxy radio luminosity per unit frequency to be proportional to the

<sup>1</sup> Recent studies (Acharya et al. 2023; Cyr et al. 2024) indicate that soft photon heating may alter the shape and amplitude of the 21-cm signal in presence of a radio background during the cosmic dawn. However, this effect is not accounted for in this work, as the analyses were conducted prior to those publications. We intend to include this effect in future work.

star formation rate (SFR):

$$L_{\text{Radio}}(\nu, z) = f_{\text{Radio}} \times 10^{22} \left( \frac{\nu}{150 \text{ MHz}} \right)^{-\alpha_{\text{Radio}}} \left( \frac{\text{SFR}}{M_{\odot} \text{ yr}^{-1}} \right) \text{ W Hz}^{-1}, \quad (6)$$

where SFR is the star formation rate, the spectral index in the radio band  $\alpha_{\text{Radio}}$  is set to the typical value of 0.7 (Mirocha & Furlanetto 2019; Gürkan et al. 2018) and  $f_{\text{Radio}}$  is the normalization of the radio emissivity. A value of  $f_{\text{Radio}} = 1$  corresponds to present day star-forming galaxies. Thus, the eight free parameters for the galactic radio models are:  $f_{\star}$ ,  $V_C$ ,  $f_X$ ,  $\alpha$ ,  $E_{\text{min}}$ ,  $\tau$ ,  $R_{\text{mfp}}$ , and  $f_{\text{Radio}}$ .

Although both an external and a galactic radio excess has an impact on the 21-cm signal, resulting in a significant enhancement of the signal during cosmic dawn and the epoch of reionization, there are notable distinctions between the two models. The spatially uniform external radio background is expected to be present during the early cosmic epochs prior to cosmic dawn, and its strength decreases with cosmic time. In contrast, the excess radio background from high redshift galaxies is inhomogeneous and its intensity increases with cosmic time as it traces the formation and growth of galaxies, assuming that  $f_{\text{Radio}}$  remains constant with redshift. We expect these differences to give an ANN a chance to distinguish signatures of these radio backgrounds in the simulated 21-cm signals.

### 3 METHODS

#### 3.1 Methods to generate the datasets

We generate the 21-cm signal as a function of astrophysical parameters across a wide range of redshifts using our semi-numerical simulation code, 21cmSPACE. For a large number of astrophysical models, we create mock 21-cm signals using the simulation and calculate the corresponding 21-cm power spectrum and global signal for each parameter combination. The parameters are sampled using randomly selected values across wide ranges of possible values in the seven-parameter space. We use three different datasets for our analysis in this paper. One dataset is generated under the assumption of the standard astrophysical scenario. In addition, we include two datasets of the 21-cm power spectrum and corresponding global signal for models that incorporate an excess radio background (either galactic or external). The dataset for the standard astrophysical scenario (without an excess radio background) includes 21-cm power spectra and global signals for 3195 models, covering a broad range of the seven astrophysical parameters, as detailed in Section 2.1. The datasets with an excess radio background, where the number of free parameters increases from seven to eight, consist of 10158 models (with a galactic radio background) and 5077 models (with an external radio background). However, to avoid any classification biases during the training process, we use a similar number of models (approximately 3,000 randomly selected models from each category) for the classification analysis. To simulate a more realistic observational scenario, we also generate one more dataset of 21-cm power spectra with expected observational effects from an SKA-like experiment, referred to as ‘mock SKA data’ (as explained in Section 3.2). Our full simulated redshift range (for the global signal and power spectrum) is  $z = 6 - 35$ , with 30 redshift bins ( $\Delta z = 1$ ). For the theoretical power spectrum (without observational effects) we use 32  $k$  bins that cover the range  $0.0492$  to  $1.095 \text{ Mpc}^{-1}$ .

#### 3.2 Mock observational datasets

In order to consider more realistic cases, we include several expected observational effects in the 21-cm power spectrum. In order to generate the mock SKA dataset, we process the direct output of the simulation using the following prescription: (a) Two-dimensional slices of simulation boxes (images) are smoothed with a two-dimensional Gaussian that corresponds to the effect of SKA resolution. (b) We add a pure Gaussian noise (smoothed with the SKA resolution) to the image as a realization of the SKA thermal noise. (c) We adopt a mild foreground avoidance to mitigate the foreground effects following Reis et al. (2022) (see also Datta et al. 2010; Dillon et al. 2014; Pober et al. 2014; Pober 2015; Jensen et al. 2015). The expected redshift dependence of these three effects is included. By mild foreground avoidance we mean that the wedge-like region that is avoided in  $k$ -space is relatively small, since we assume that the SKA will enable a reasonably accurate foreground removal as a first step of foreground mitigation. For the ‘mock SKA data’, we utilize eight redshift bins (covering  $z = 6 - 27.4$ ) and five  $k$  bins (covering  $k = 0.05 \text{ Mpc}^{-1}$  to  $1 \text{ Mpc}^{-1}$ ). At each redshift, we calculate the mean of the 21-cm power spectrum over the range of  $k$  values within each  $k$ -bin. This procedure is applied to all models in the mock SKA dataset (for more details, see Sikder et al. 2024a).

To create a realistic dataset for the global 21-cm signal, we introduce random Gaussian noise to the ideal global signal generated by the simulation. Specifically, to the signal in each redshift bin ( $\Delta z = 1$ ) we add Gaussian noise with mean  $\mu = 0$  and  $\sigma$  of 2.5 mK, 17 mK, or 25 mK, resulting in three levels of noisy global 21-cm signal datasets. The 17 mK and 25 mK noise levels correspond to the range of typical sensitivity of existing telescopes (Bowman et al. 2018; de Lera Acedo et al. 2022), while the 2.5 mK level is an optimistic scenario that represents the sensitivity of a next-generation global signal telescope. Below we sometimes also restrict the considered redshift range when considering various specific experiments.

#### 3.3 ANN, hyper-parameter tuning, & data pre-processing

In this section we describe the basic structure of our ANN, followed by the steps we take for hyper-parameter tuning and data pre-processing. The main ingredients of an ANN are as follows. Each neural network has three different types of layers - input layer, hidden layer and output layer. Each layer consists of a set of neurons or nodes. Each neuron has inputs and a single output that can serve as the input for other neurons. We use a supervised learning algorithm, namely the Multi-layer Perceptron (MLP, Ramchoun et al. 2016) from the Scikit-learn library (Pedregosa et al. 2011), for our analysis. The MLP can be used for both regression and classification problems and is trained using the backpropagation algorithm (Rumelhart et al. 1986). In regression problems, the mean square error loss function is used, while in classification tasks, the loss function is the Average Cross-Entropy. Starting with randomly chosen initial weights, the MLP minimizes the loss function, typically using a gradient descent technique, by repeatedly updating the weights from the outermost layer to the input layer. The algorithm terminates once it either reaches the maximum number of iterations or the improvement in the loss function falls below a predetermined threshold.

Although an MLP has the capability to learn highly non-linear models, it is sensitive to feature scaling and requires tuning several hyper-parameters. In an ANN, hyper-parameters are those that cannot be optimized during the training process. These include the number of hidden layers, the number of nodes/neurons in each layer, the activation function for hidden layers, and the solver for weight optimization.



To perform hyper-parameter tuning, we use *GridSearchCV*, which exhaustively searches all parameter combinations over a specified grid, fits the model, and retains the best combination of hyper-parameters.

Data pre-processing is a crucial step in enhancing the performance of an ANN. One common requirement for most of the machine learning estimators is dataset standardization, which ensures that the estimators behave properly. Mathematically, this involves subtracting the mean from each feature value and then dividing by the standard deviation, making the features resemble a standard normal distribution with a mean of zero and unit variance. The *Scikit-learn* library (Pedregosa et al. 2011) provides several utility functions for standardization. In this work, we use either *StandardScaler* or *QuantileTransformer* to standardize different datasets. In each category of data (global signal, clean power spectrum, and mock SKA power spectrum), standardization was done once, on all the models in the training datasets (from the various classes of models). Standardization on the combined datasets preserves the information on the relative amplitudes of the different model classes. We chose the utility function in each case that gave the highest classification accuracy.

Although we use all the available dimensions of the power spectrum datasets for classification, we reduce the dimensionality of these datasets when reconstructing the power spectrum from the global 21-cm signal. For dimensionality reduction, we employ the fast, unsupervised algorithm known as Principal Component Analysis (PCA) (Jolliffe & Cadima 2016) as a second step in data pre-processing. PCA projects the data into a lower dimensional space that preserves a maximum variance in the data. The first principle component captures the maximum variance in the data, the second captures the next highest variance, and so forth. Selecting too many principal components can lead to overfitting, where the model becomes too specialized with respect to the training data and fails to generalize well to new data. Therefore, it is important to set the appropriate number of principal components. We determine the optimal number of principal components based on two regression performance metrics: the  $R^2$  score and mean squared error (MSE), using functions from the *Scikit-learn* metrics module. Details on the number of PCA components used for signal reconstructions (either the power spectrum or global signal) are provided later (in sections 5.1 and 5.2). The specific network architecture and data pre-processing steps used for each network are also discussed in the following section.

## 4 CLASSIFICATION OF THE RADIO BACKGROUND

### 4.1 Classification using the ideal dataset

As noted above, in this work we employ standard astrophysical models (CMB background only) along with both excess radio background models (galactic and external). We train an ANN classifier to distinguish the type of radio background present in the signal. The test dataset consists of a total of 900 models, with 300 models from each category. To select the excess radio models for the test dataset, we follow this approach:

(i) In the test dataset, we excluded the most extreme EDGES-motivated models (as were considered, e.g., in Sikder et al. 2024a) and instead focused on models with moderate excess radio backgrounds, since such backgrounds might be realized in nature with a population of radio galaxies that is relatively similar to that expected in a normal astrophysical scenario. To this end, we set the maximum limit for  $f_{\text{Radio}}$  in the galactic radio background models,  $f_{\text{Radio,max}}$ , to 300.

(ii) To make things more difficult and realistic for the classifier,

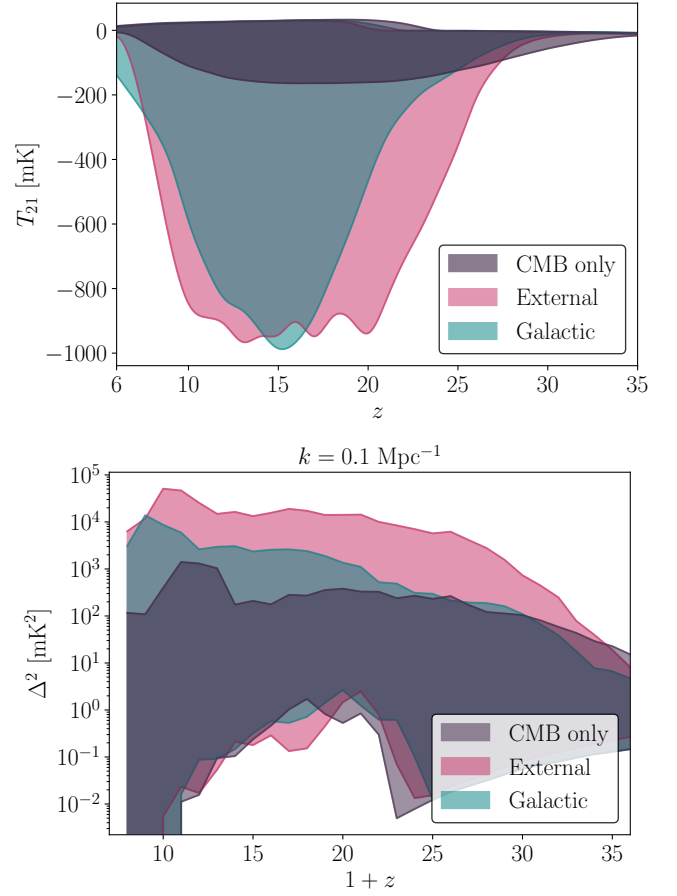


**Figure 1. Top panel:** The global signal envelopes for the three different classes of models included in our test dataset for classification. **Bottom panel:** The envelopes for the 21-cm power spectrum at  $k = 0.1 \text{ Mpc}^{-1}$ . Here we show the theoretical 21-cm signal, without any observational effects.

we wanted to ensure that the test datasets with the two different radio backgrounds have a similar range of global signals. Thus, we set a maximum depth ( $T_{21,\text{max}}$ ) of the global signal. To find this value quickly, we identified galactic models for which  $f_{\star} > 0.35$ ,  $V_c < 10 \text{ km s}^{-1}$  and  $f_{\text{Radio}} < f_{\text{Radio,max}}$ . These criteria for  $f_{\star}$  and  $V_c$  were used to select models with efficient early star formation, leading to efficient Lyman- $\alpha$  coupling, which results in deeper absorption troughs in the global signal.

(iii) We randomly selected 300 models from a subset (897 models) of the entire galactic models, for which  $f_{\text{Radio}} < f_{\text{Radio,max}}$  and the absorption trough in the global signal is shallower than  $T_{21,\text{max}}$ .

(iv) Next, we identified the max value of  $A_r$ ,  $A_{r,\text{max}}$ , of the external models that gives a global signal absorption trough just under  $T_{21,\text{max}}$ . For this, we considered only external models where  $f_X < 0.001$ , giving very low X-ray heating and thus strong absorption.

(v) Finally, we randomly selected 300 models from a subset (3070 models) of the entire dataset of external radio models, for which  $A_r < A_{r,\text{max}}$  and the absorption trough in the global signal is shallower than  $T_{21,\text{max}}$ .

Having thus selected the test data, we create a training dataset comprising 8,893 models, including 2,893 models with the CMB-only background, 3,000 models with an excess external radio background, and 3,000 models with an excess galactic radio background. These

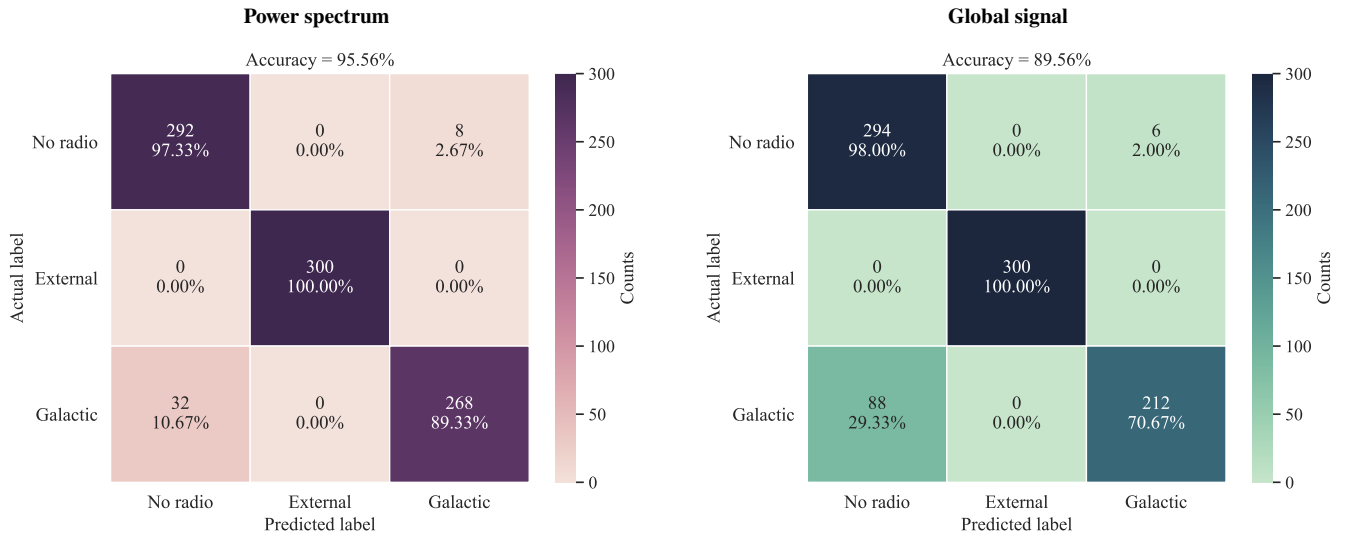


**Figure 2.** **Left panel:** The confusion matrix shows the performance of classifying various radio backgrounds given the 21-cm power spectrum without any observational effects. The model classes were ‘No radio’ (the standard astrophysical scenario without any excess radio background, i.e., CMB only), external radio models, and galactic radio models. The percentages add to 100 in each row, which corresponds to a particular true model class. Each column corresponds to a particular model class as predicted by the classifier. **Right panel:** A similar confusion matrix, but showing the performance of the classification procedure based on the global 21-cm signal (without any observational noise).

were chosen randomly out of our full sets of the various models (after excluding the models in the test data). Thus, the training data had roughly the same number of models of each class, and covered their full ranges, so the ANN did not know at the training stage that the test data of the two excess radio models would be constrained to have similar global signal ranges.

In Fig. 1 we present the envelopes of the global signal and power spectrum for the test data of the three different classes of models (CMB only, external, and galactic radio backgrounds). The models in the test dataset were excluded from the training dataset, meaning that the ANN classifier did not encounter these test models during hyperparameter tuning and training. Therefore, the performance analysis using the test dataset provides a reasonable estimate of the network’s prediction accuracy. For classification, we label the models as “0” for CMB only (no excess radio), “1” for external excess radio models, and “2” for galactic excess radio models.

To construct an ANN classifier that uses the 21-cm power spectrum as the input, we employ a five-layer MLP (input layer, three hidden layers and output layer), with 134 neurons in each hidden layer. We transform the power spectrum dataset to a logarithmic scale ( $\log_{10}$ ) and standardize it using the *StandardScaler* class from the *Scikit-learn* library (Pedregosa et al. 2011). The activation function for the hidden layers is chosen to be a *rectified linear unit* function (ReLU, Nair & Hinton 2010), and a stochastic gradient-based optimizer, namely the *adam* optimizer (Kingma & Ba 2014), is applied for weight optimization. For the network that uses the global signal as input to predict the type of radio background, we use a single hidden layer with 143 neurons. The global signal dataset is standardized using the *QuantileTransformer* method, which transforms features to follow a normal distribution based on quantile information. This network uses the *logistic sigmoid* function (Han & Moraga 1995) as the activation function and the same weight optimizer as the power spectrum-based network. Due to the stochastic nature of the training process, different runs of the same model on the same dataset can produce slightly different results. To ensure reliability, we train each ANN classifier 40 times with a fixed network

architecture, as determined after hyperparameter tuning, and calculate the mode of predictions across these runs to evaluate the final classification accuracy.

The performance of our classification procedure is shown using confusion matrices in Fig. 2. The left panel of Fig. 2 presents the classification results for various radio backgrounds based on the 21-cm power spectrum without observational noise. Among 300 models with no excess radio background, only 2.7% were incorrectly classified as having a galactic radio background. For 300 true external radio models, there were no mis-classifications. However, for true galactic radio models, 11% were incorrectly classified as having no excess radio. The overall classification accuracy using the 21-cm power spectrum across a wide range of redshifts and wavenumbers was 96%. The right panel of Fig. 2 shows the classification performance based on the global signal. For true standard astrophysical models, only 2.0% of models were misclassified as having a galactic radio background, while for true external models, the ANN classifier achieved 100% accuracy. For true galactic radio models, the network misclassified 29% as having no excess radio. The overall classification accuracy in this case was 90%.

Even when we use a dataset without observational noise, there is still some effective uncertainty due to the limited sampling of the large multi-dimensional parameter space of each model. The higher accuracy in using the power spectrum is likely due to the greater degree of information that is available in this case. It is evident that models with an external radio excess can be classified with significantly higher accuracy (100% based on either the power spectrum or global signal). However, a significant fraction of galactic models were misclassified as having no excess radio. This is likely because in the galactic radio model, the radio emission follows the overall redshift evolution of star formation, like other radiation outputs that are also present in the standard astrophysical model. On the other hand, the external radio excess (see eq. 5) is not of astrophysical origin and has a substantially different redshift evolution (as it is especially enhanced at high redshifts), and can therefore be more easily identified. We note that the results are driven by the detailed shapes

(with respect to redshift and, for the power spectrum, wavenumber), not just overall signal amplitudes. For example, in the case of the global signal, 60% of test-data galactic models fall within the maximum depth of standard (no radio) models (164 mK depth), along with 21% of external models. The misclassification rates are much lower than these fractions. In the case of the power spectrum, 93% of test-data galactic models fall within the maximum height of standard models ( $1.4 \times 10^3 \text{ mK}^2$ ), along with 40% of external models. We also note that the mis-classification of Galactic as No radio occurs much more frequently than the reverse; this asymmetry is likely affected by the test data for the Galactic models covering only a part of the range of the Galactic training data, while the classifier effectively compares a given model to the model class as characterized by the entire training set. We further explore the dependence on amplitude in section 4.3 below.

These results indicate that both ANN classifiers could potentially distinguish external radio excess from galactic radio background models and standard astrophysical models if such an excess is present in the observed 21-cm power spectrum and global 21-cm signal. We note that, up to this point, we have used the simulated global 21-cm signal and power spectrum without any observational effects for training and testing the classifiers. In a more realistic observational scenario, several challenges arise. In the next subsection (4.2), we present our analysis based on mock realistic datasets.

#### 4.2 Classification using realistic mock datasets

To assess the performance of the classification procedure in a more realistic scenario, we trained an ANN classifier using mock SKA 21-cm power spectra. We adopted the same activation function and weight optimizer as in the noiseless case, but here we standardized the mock SKA power spectra dataset using the *QuantileTransformer* scheme and utilized three hidden layers with 200 neurons each. The left panel of Fig. 3 displays the confusion matrix summarizing the classification results based on the mock SKA 21-cm power spectra. Of the 300 models with no excess radio background, 8% were misclassified as having an excess radio background. For the 300 models with an external radio background, 88% were correctly classified, while 69% of true galactic radio models were accurately predicted to have the correct type of radio excess. We found that including various expected observational effects in the power spectra led to a lower overall classification accuracy of 83%, compared to 96% in the case without any observational noise. The reduction in accuracy can be attributed to the observational effects as also reflected in having fewer  $k$  and  $z$  bins available for the 21-cm power spectra with mock SKA features. While the galactic radio case is most affected (in terms of the change in the percentages), the external radio case is also significantly affected, as the SKA observational effects are strongest at the highest redshifts.

For a realistic assessment of our classification procedure using the global signal, we added random Gaussian noise to the ideal global 21-cm signal from the simulation, in order to account for the sensitivity of various global signal telescopes (and analysis pipelines). We then constructed an ANN classifier using a similar architecture as the network that used the global signal without observational noise. The right panel of Fig. 3 presents the classification performance for one of three different noise levels—specifically, an optimistic level of random Gaussian noise (with  $\sigma = 2.5 \text{ mK}$  and  $\mu = 0$ ) added to the simulated sky-averaged signal. The classifier in this case achieved an overall accuracy of 79% in identifying the type of radio background. Since the classifier determines the radio background type based on the shape and amplitude of the global signal, the added random

Bin number	Range in mK	# of samples in test set
1	[0, -50]	120 + 120 + 120
2	[-50, -100]	120 + 120 + 120
3	[-100, -150]	120 + 120 + 120
4	[-150, -200]	120 + 120 + 120
5	[-200, -250]	120 + 120
6	[-250, -300]	120 + 120
7	[-300, -350]	120 + 120
8	[-350, -400]	120 + 120
9	[-400, -450]	120 + 120
10	[-450, -500]	120 + 120

**Table 1.** Amplitude ranges (in mK) of the absorption troughs considered in 10 bins. For each amplitude bin, we selected 120 samples from each class, resulting in a total of 360 samples per test dataset. Since the maximum absorption trough depth for the standard (No radio) model is approximately -165 mK, for bins greater than 4 we only use external and galactic models with maximum absorption depth corresponding to the particular bin.

Gaussian noise complicates the learning algorithm’s ability to track the shape and altered amplitude, resulting in reduced classification accuracy. Higher Gaussian noise levels with  $\sigma$  values of 17 and 25 mK yielded significantly lower classification accuracies due to substantial distortion in the global signal’s shape and amplitude (see Fig. B1). The standard model class still achieves 91% accuracy, but the Galactic radio class is around 40% and even the External radio class is down to  $\sim 60\%$ . The classification is mainly enabled by the distinct behavior at high redshifts, as we discuss later; at the high-redshift end, the signal amplitude is relatively low, making it more susceptible to the added noise. Inferring the type of radio background from datasets of existing telescopes will be challenging unless the observed signal shows a significantly enhanced radio background compared to the standard astrophysical model.

#### 4.3 The dependence of radio background classification on global signal amplitude

To explore how the depth of the global signal absorption trough affects the classification accuracy, we divided the data (for the case without observational noise) into 10 separate bins based on the trough depth. The amplitude ranges for each bin are listed in Table 1. For this analysis, we set an upper limit of -500 mK for the absorption amplitude, aligning with the best-fit amplitude suggested by the purported EDGES detection (Bowman et al. 2018). Each bin represents a distinct test dataset containing 360 samples, composed of 120 randomly selected global signal samples from each class, where the absorption troughs fall within the specific range of the bin (except that bins that are beyond the range of No radio models do not contain this class). These test datasets are then applied to the trained classifier to evaluate the classification accuracy. Fig. 4 shows the variation in classification accuracy as a function of the global signal amplitude (where a higher bin number indicates a deeper absorption trough). Deeper absorption troughs lead to more accurate classification of the excess radio models. For the galactic model in particular, the accuracy for bins 5 and up is significantly higher than for the first 4 bins, which suggests that once the absorption depth exceeds values expected from standard astrophysical scenarios, the depth itself becomes a key factor in distinguishing between excess radio models and standard models. However, even for the first 4 bins, the classification accuracy is fairly high for all model classes, especially for the external radio background. We note that Fig. 4 does not exactly

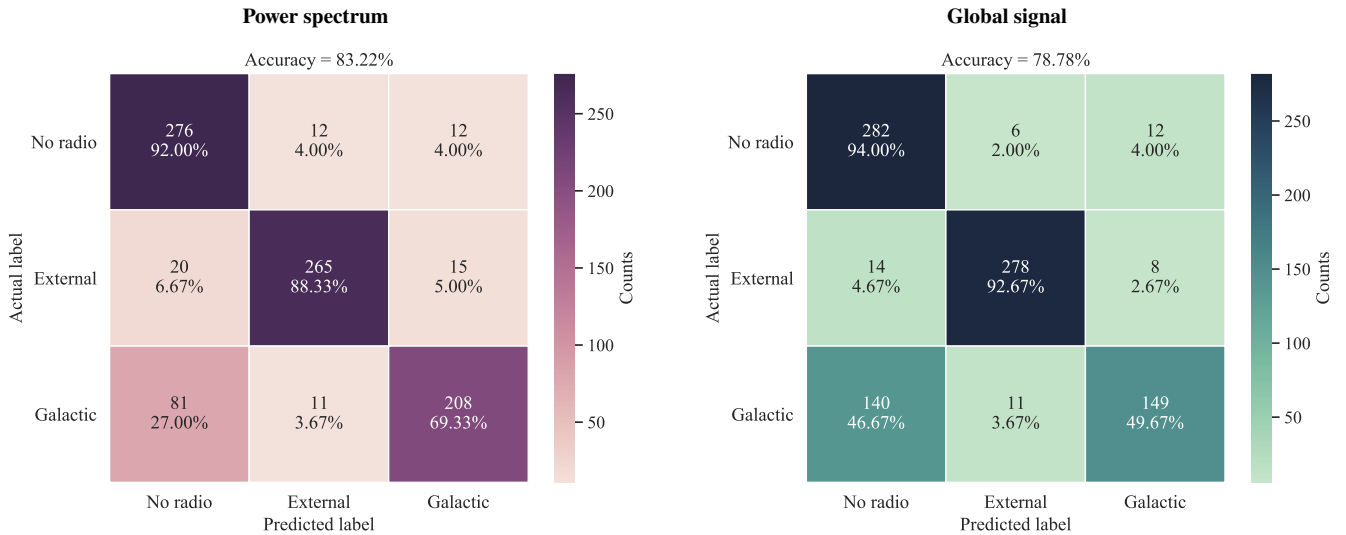


**Figure 3. Left panel:** The confusion matrix shows the performance of classifying various radio backgrounds given mock SKA 21-cm power spectra. The setup and notation is the same as in Fig. 2. **Right panel:** A similar confusion matrix, but illustrating the classification performance using the global signal with random Gaussian noise. Here, we show the classification performance for a relatively low noise level: a random Gaussian noise with  $\mu = 0$  and  $\sigma = 2.5$  mK. The performances for additional noise levels ( $\sigma = 17$  mK and 25 mK) are shown in Fig. B1.

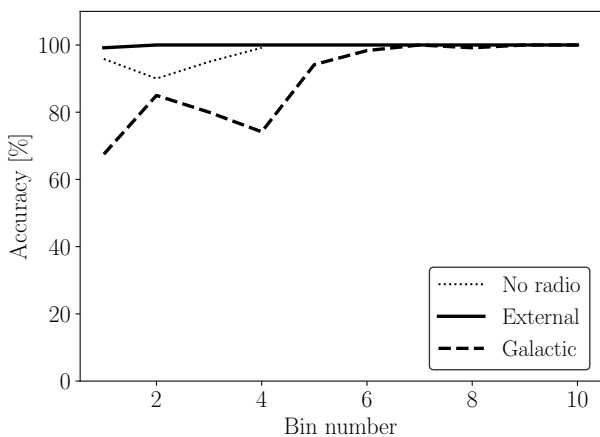


**Figure 4.** Classification accuracy as a function of the amplitude of the global signal absorption trough (without observational noise). The higher the bin number, the higher is the signal amplitude (see Table 1 for the amplitude range of each bin).

correspond to the results in section 4.1 since here the various models were selected from the full datasets with only a restriction on the amplitude.

To help understand why the classification of the external radio background is so effective, we conducted an additional analysis. We selected both external and galactic radio models from our training dataset and statistically evaluated the differences in their brightness temperature distributions at each redshift. We quantified this distinction using a statistical distance metric known as the total variation distance (TVD), which measures the maximum difference between two distributions. The TVD is related to the L1-norm and defined by the equation (Levin et al. 2006):

$$\text{TVD} = \frac{1}{2} \sum_i |P_i - Q_i|, \quad (7)$$

where  $P$  and  $Q$  represent the two distributions, and  $i$  is the bin

number. A TVD value of zero indicates that the two distributions are identical, while a TVD value of 1 suggests complete dissimilarity between the normalized distributions. Higher TVD values reflect greater differences between the distributions. We calculated the TVD at each redshift, and its evolution with redshift is shown in Fig. 5. Below redshift 27, the TVD hovers around or below 0.2. However, beyond this point, the TVD rapidly increases with redshift, indicating significant differences between the temperature distributions of the external and galactic models at redshifts greater than 27. The inset plots in Fig. 5 compare the normalized temperature distributions of the galactic and external models at  $z = 17$  and 32. While the distributions are similar at  $z = 17$ , they diverge significantly at  $z = 32$ . These high redshift differences could potentially account for the accurate classification of the external radio background, regardless of the global signal amplitude. In the next subsection we further explore various scenarios by selecting distinct redshift ranges for training and subsequently calculating accuracy scores for the same test dataset.

#### 4.4 Classifications using REACH and SARAS 3 bands

In this subsection, we consider the redshift intervals covered by global signal experiments like REACH ( $z : 7 - 28$ ) (de Lera Acedo et al. 2022) and SARAS 3 ( $z : 15 - 25$ ) (Bevins et al. 2022). We train the classifier using simulated global signal data specific to these redshift ranges and then replicate the analysis performed in 4.3. For this analysis, we utilize the simulated global signal data without any added Gaussian random noise. Fig. 6 shows the variation in accuracy with the depth of the absorption troughs for both the REACH (dark blue lines) and SARAS 3 (dark orange lines) redshift bands.

For the REACH band, the classification accuracy is generally similar to that shown found for the full redshift range in Fig. 4. The only significant difference occurs for the external radio model. This reaffirms the notion highlighted in the previous section that very high-redshift signal information is important for accurately distinguishing external models from the other two categories. Still, the accuracy for classifying the various model classes is high, even for low absorp-



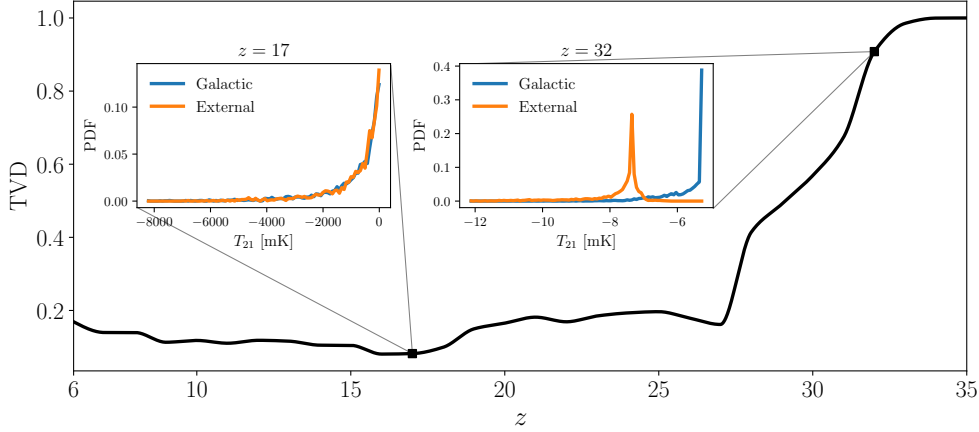


**Figure 5.** The total variation distance (TVD) as a function of  $z$  between the normalized PDFs of the global signals (without observational noise) of galactic and external models in the training dataset. TVD quantifies the difference between two probability distributions (see text). The inset plots show the normalized PDFs of the sky averaged 21-cm brightness temperatures from galactic and external models (all models in the training sets) at  $z = 17$  and  $32$ . At lower redshifts ( $< 27$ ), the value of the TVD is low compared to that at high redshifts, indicating that the difference between the normalized PDFs from galactic and external samples is much larger at high redshifts. Thus, the high-redshift behavior of external models is likely the reason behind the accurate classification of those models relative to the other two models, irrespective of the overall global signal amplitude.

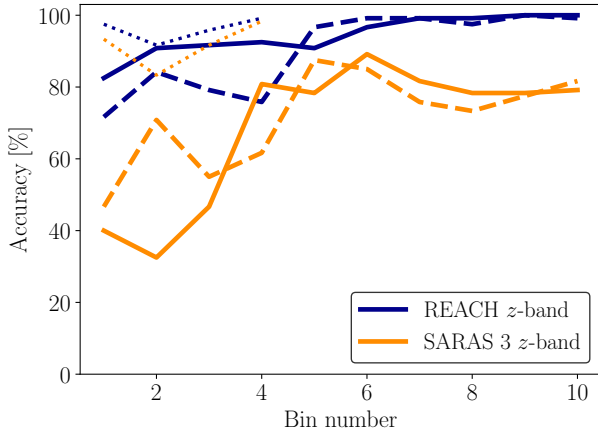


**Figure 6.** Same as Fig. 4, but here we consider only the accessible redshift range of the REACH or SARAS 3 experiment when we train the classifier for excess radio background model classification.

tion amplitudes. This indicates that global signal observations from REACH-like experiments have the potential to detect the presence or absence of an external radio background in the 21-cm signal. The narrower redshift range of the SARAS 3 band results in lower classification accuracies. Again, the largest effect is on the External radio model, so that its accuracy becomes similar to that of the Galactic radio model. At low amplitudes that are within the range of standard astrophysical models, the excess radio models have a classification accuracy comparable to 50% with the SARAS 3 redshift range, while the accuracy is still high ( $\sim 80\%$ ) at higher absorption amplitudes.

## 5 MAPPING 21-CM OBSERVABLES: THE GLOBAL SIGNAL AND THE 21-CM POWER SPECTRUM

While previous studies in the literature have utilized ANN to construct emulators for the power spectrum and global signals, aiming to estimate the astrophysical parameters of cosmic dawn and the EoR,

here we first apply an ANN for the direct mapping of the two key observables in 21-cm cosmology: the global signal, which could potentially be observed using a single radio antenna, and the 21-cm power spectrum, a statistical measurement through radio interferometry. Traditionally, the emulation approach involves obtaining data for one of these observables and then employing these data to constrain the underlying astrophysical model. Subsequently, with the help of the determined astrophysical model, predictions can be made for the other observable, utilizing machine learning algorithms proposed in the existing literature. The novelty here lies in the capability of the proposed network to directly predict the feasible range of one observable when provided with observations of the other. This streamlined approach represents a potentially useful and efficient way to analyze 21-cm cosmology data from upcoming experiments.

### 5.1 Prediction of the global 21-cm signal

#### 5.1.1 Method

It is interesting to validate the consistency of the signals obtained from interferometers and radiometers. To do so, we construct an ANN to predict the global signal over a wide range of redshifts given the 21-cm power spectrum over the same redshift range. This also depends on the classification into different model classes. Here, as a proof of concept, we use only the datasets with standard astrophysical models (no excess radio, i.e., CMB only). The network has three hidden layers with 150 neurons or nodes in each layer. We express the dataset of the 21-cm power spectrum in log scale before applying it to the training procedure. To do one of the preprocessing steps, i.e., standardization of the features, we use the *StandardScaler* class from the *Scikit-learn* library (Pedregosa et al. 2011). After the standardization of the dataset, all the features have a zero mean and unit standard deviation. The next data preprocessing step involves projecting the dataset into a lower dimensional space using PCA. To find the optimal number of PCA components, we train the network with a fixed network architecture for various choices of PCA components, apply the trained network on the test dataset, and calculate the  $R^2$  score and the mean squared error (MSE) in predicting the global signal. The  $R^2$  score quantifies the goodness of fit so that an  $R^2$

score = 1 implies a perfect fitting. The lower the MSE is, the better is the fitting quality. We select the number of PCA components to be 100 as we found that 100 PCA components yields the maximum  $R^2$  score and minimum MSE (see Fig. A1). Thus, the network has a 100 dimensional input layer and the dimension of the output layer is 30 as it reconstructs the global signal at 30 redshifts ranging from 6 to 35. We use the ReLU as the activation function for the hidden layers and choose the *adam* optimizer for weight optimization of the network. Once the network is trained, we apply it to the test dataset for predictions.

In order to understand the performance of the prediction when using the 21-cm power spectrum with observational noise, we also train a network that can predict the global signal given the mock SKA 21-cm power spectrum. We use the same network architecture and same preprocessing steps except that here we do not apply PCA to project the dataset into a lower dimensional space, because in this case, we already use the 21-cm power spectrum binned over 8  $z$  and 5  $k$  values. Thus, the dimension of the input dataset is already reduced by a factor of 20 compared to our noise-less dataset.

### 5.1.2 Performance analysis

We evaluate the overall performance of the network in predicting the global 21-cm signal given the power spectrum using the following equation, where we define the error as the r.m.s. value of the difference between the predicted global signal ( $T_{\text{Predicted}}$ ) and the true global signal ( $T_{\text{True}}$ ) from the simulation with the same parameter set, normalized by the maximum amplitude of the true global signal:

$$\text{Error} = \frac{\sqrt{\text{mean} [(T_{\text{True}}(z) - T_{\text{Predicted}}(z))^2]}}{\max |T_{\text{True}}(z)|}. \quad (8)$$

For a test dataset of 300 standard astrophysical models, the median value of the error is 0.0094. Also, 95% of cases have an error less than 0.061, which shows that the quality of the prediction is generally high. The predicted global signal deviates more from the actual one when the absorption trough is shallower; we note that these signals would be more challenging to detect in the first place owing to the limited telescope sensitivity. In Fig. 7, the dark red histogram shows the error over all the test models in the case of an ideal detection without instrumental/foreground effects. We show a few specific examples of predicting the global signal from the ANN trained using the power spectrum without any observational effects in the left panels of Fig. 8: 10'th percentile error (0.004, top panel), median error (0.010, middle panel) and 90'th percentile error (0.043, bottom panel). In each panel, the solid blue and red lines show the predicted and true global signal for the same astrophysical model parameters. It is evident from the bottom panel that even in the case of the 90'th percentile error, the location of the features was predicted well. Thus, given a noise-free power spectrum we can reconstruct the corresponding global signal quite well, and the error in reconstruction is very small compared to the astrophysical uncertainty in the signal (illustrated by the scatter of gray lines).

If we use a mock SKA 21-cm power spectrum to predict the global signal using the trained network, we find that although this power spectrum includes several observational effects and is calculated over a smaller number of  $z$  and  $k$ -bins, the trained network can still effectively reconstruct the global signal with good accuracy. The gray histogram in Fig. 7 shows the error over a test dataset of 300 models in predicting the global signal given the mock SKA power spectrum. Here the median error is 0.035 and the error is less than 0.33 for 95%

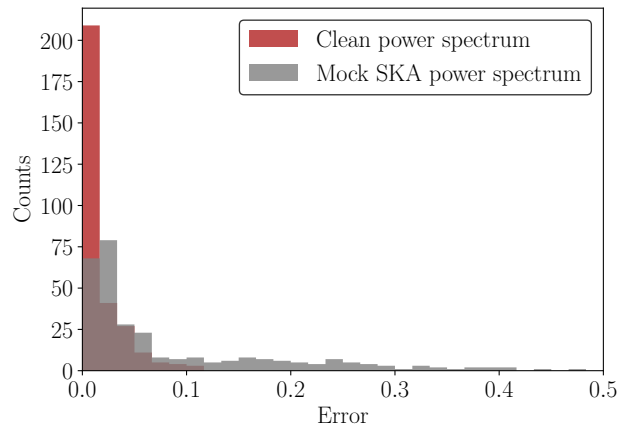


**Figure 7.** Histogram of the relative error in the global signal predicted based on a given power spectrum, where the relative error is defined by equation 8. When the network is trained using the clean power spectrum, the median error in predicting the global signal is 0.0094, while for the network trained using a mock SKA power spectrum, the median error is 0.035. Here we use models that assume the standard astrophysical scenario (CMB only).

of test cases. We also show a few specific examples that compare the predicted and true global signal for the same set of astrophysical parameters in the right panels of Fig. 8: 10'th percentile error (0.012, top panel), median error (0.035, middle panel) and 90'th percentile error (0.25, bottom panel). We find that the prediction is still fairly accurate, unless the absorption trough is shallow (well below 100 mK in depth).

## 5.2 Reconstruction of the 21-cm power spectrum

### 5.2.1 Method

Here we attempt to do the reverse of the previous subsection. In order to map between the 21-cm power spectrum and global signal, we construct an ANN that is able to predict the 21-cm power spectrum over a wide range of redshifts and wavenumbers given the global signal over a similar range of redshifts. The network architecture comprises four hidden layers, each containing 300 neurons. Similar to the network discussed previously, data preprocessing steps include transforming the power spectrum dataset to a logarithmic scale, standardizing it using Scikit-learn's StandardScaler, and reducing its dimensionality with PCA. After comparing the  $R^2$  score and MSE for various choices of PCA components, we select 22 PCA components, since this yields the highest  $R^2$  score and the lowest MSE. Consequently, the network features a 30-dimensional input layer, representing the global signal at 30 different redshifts, and a 22-dimensional output layer. By incorporating the dimensionally reduced power spectrum dataset into the learning algorithm, the network effectively captures the overall signal across a broad redshift range (from 6 to 35). The original dimensions are then reconstructed using an inverse PCA transformation as a post-processing step. As a result, a reasonably good prediction accuracy is achieved. The network employs ReLU as the activation function for the hidden layers and the *adam* optimizer for weight optimization.

### 5.2.2 Performance analysis

In order to examine the overall performance in reconstructing the power spectrum, we use a test dataset of 300 models that were not

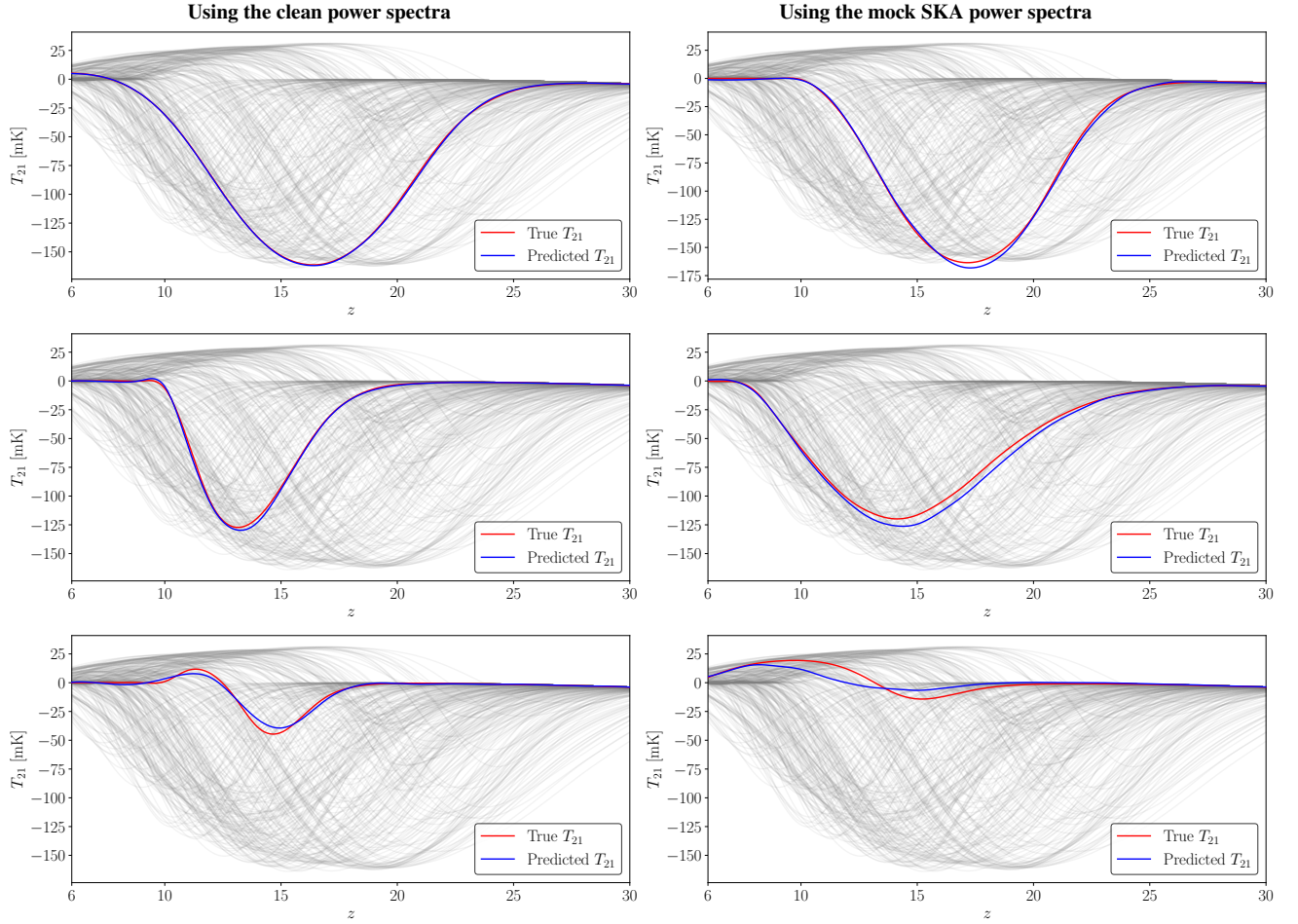


**Figure 8.** Comparison between the true (red curve) and predicted (blue curve) global 21-cm signal. Different models shown here illustrate particular percentiles of the error when reconstructing the global signal based on the power spectrum, either with or without various observational effects. The gray lines in each panel show all the samples in the test dataset. **Left panels:** Here we use the clean power spectrum without any observational effects. The error illustrated by the model in each panel is as follows: Top: 10<sup>th</sup> percentile error (0.004), middle: median error (0.010), and bottom: 90<sup>th</sup> percentile error (0.043). The error is less than 0.061 for 95% of cases. **Right panels:** Here we reconstruct the global signal using the mock SKA power spectrum. The error for each of the panels is as follows: Top: 10<sup>th</sup> percentile error (0.012), middle: median error (0.035), and bottom: 90<sup>th</sup> percentile error (0.250).

part of the training dataset. We define the error as the r.m.s. value of the difference between the predicted power spectrum ( $\Delta_{\text{predicted}}^2$ ) and the true power spectrum ( $\Delta_{\text{true}}^2$ ) generated from the simulation for the same parameter set, normalized by the maximum value of the true power spectrum over all  $k$  and  $z$ :

$$\text{Error} = \frac{\sqrt{\text{Mean} \left[ \left( \Delta_{\text{predicted}}^2 - \Delta_{\text{true}}^2 \right)^2 \right]}}{\text{Max} \left[ \Delta_{\text{true}}^2 \right]}. \quad (9)$$

Here the mean is taken over all  $k$  and  $z$  bins. We show the histogram of the error in gray in the left panel of Fig. 9. The median and the mean value of the error over the entire test dataset are 0.045 and 0.052, respectively. We find that the error is less than 0.101 for 95% of cases.

To illustrate the performance of the network in reconstructing the power spectrum from a given global signal, we show several specific examples in Fig. 10: 10<sup>th</sup> percentile error (0.020, top panel), median error (0.045, middle panel), and 90<sup>th</sup> percentile error (0.092, bottom panel). In this figure we show the power spectrum at  $k = 0.4 \text{ Mpc}^{-1}$ , for illustration. We see that the prediction is generally quite good.

Here we again note that the error in reconstruction is far smaller than the scatter due to the astrophysical uncertainty.

In addition to reconstructing the power spectra within the standard astrophysical scenario, we also evaluate the overall performance in predicting the power spectra with an excess radio background over the CMB. Here we retrain the ANN separately with each class of radio backgrounds. The right panel of Fig. 9 shows the histogram of errors in predicting the power spectra given the global 21-cm signals with an excess radio background. The two histograms are shown for test datasets of 300 models with an external and galactic radio background, respectively. We find that for models with an external radio excess, the error is lower than 0.081 for 95% of test cases, while for models with a galactic radio background, the error is lower than 0.101 for 95% of test cases, which is similar to the result for the standard astrophysical scenario. The comparisons between the true and predicted power spectra with an external radio background for a few specific models is shown in Fig. C1: 10<sup>th</sup> percentile error (0.022, top panel), median error (0.044, middle panel) and 90<sup>th</sup> percentile error (0.072, bottom panel). While the network predicts the power spectrum over a wide range of wavenumbers, for illustration we show the power spectrum at  $k = 0.4 \text{ Mpc}^{-1}$ . A few specific

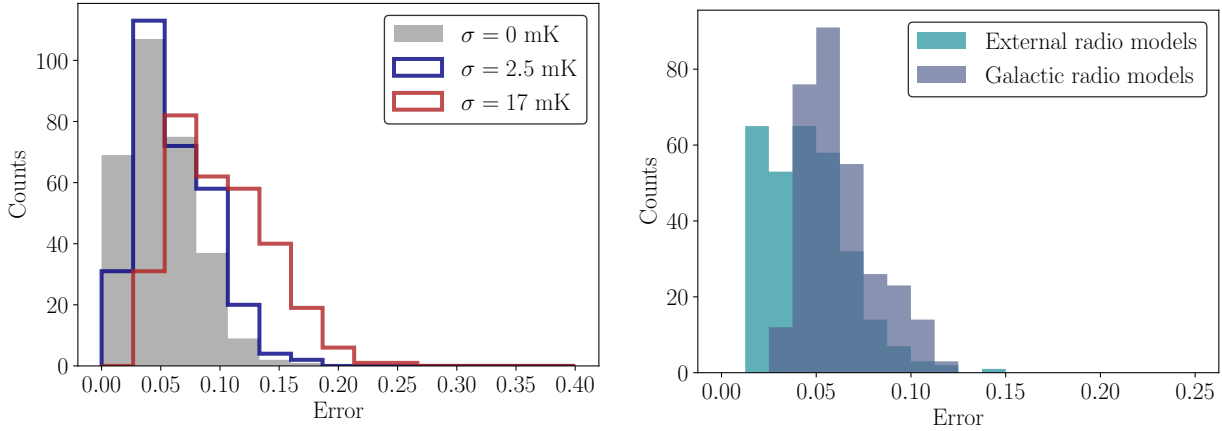


**Figure 9.** Histogram of the errors in the predicted 21-cm power spectrum as defined by equation 9. **Left panel:** The power spectra are predicted based on the global signals using three trained networks. The results are shown for a test dataset of 300 standard astrophysical models (CMB only). Here the networks are trained using global signal without any noise (gray) or with added Gaussian random noise:  $\sigma = 2.5$  mK,  $\mu = 0$  (blue) and  $\sigma = 17$  mK,  $\mu = 0$  (red). **Right panel:** The error histograms are shown in reconstructing the 21-cm power spectrum with an excess radio background. The teal and gray histograms show the error for the 300 models with an external radio background and 300 models with a galactic radio background, respectively. In both cases, we use the power spectrum without any observational noise.

Global signal	Median error	Mean error
Without any noise ( $\sigma = 0$ )	0.045	0.052
Gaussian noise with $\sigma = 2.5$ mK	0.056	0.062
Gaussian noise with $\sigma = 17$ mK	0.094	0.100

**Table 2.** Median and mean errors in predicting power spectra given global signals without or with random Gaussian noise. These errors correspond to the histograms shown in the left panel of Fig. 9.

examples of the true and predicted power spectrum with a galactic radio background are shown in Fig. C2: 10<sup>th</sup> percentile error (0.041, top panel), median error (0.058, middle panel) and 90<sup>th</sup> percentile error (0.094, bottom panel). In general, the reconstruction is reasonably good given that we are reconstructing the power spectrum over a wide range of wavenumber at each redshift using only the global signal versus redshift.

### 5.2.3 Reconstruction of the 21-cm power spectrum from a noisy global signal

In order to understand the effect of the typical uncertainty of the global signal measurement in predicting the 21-cm power spectrum, we consider networks that are trained using the global signal with added Gaussian noise. Along with the typical sensitivity of existing global signal telescopes ( $\sigma = 17$  mK), we also consider an optimistic case ( $\sigma = 2.5$  mK) for our analysis. In Fig. 9, we show histograms of errors (calculated using equation 9) in the predicted 21-cm power spectrum, based on the global signal with added Gaussian random noise. The mean and median errors for these scenarios are listed in Table 2. When compared to the gray histogram (for the noiseless case), it is clear that introducing Gaussian noise to the simulated global signal significantly increases the reconstruction error of the power spectrum. Specifically, the typical sensitivity of global signal experiments, such as the 17 mK noise level in EDGES low-band, results in a significant error, approximately 1.6 times larger than the error for an optimistic error level of 2.5 mK.

Redshift bands	Median error	Mean error
$z : 6 - 35$	0.045	0.052
$z : 7 - 28$ (REACH)	0.050	0.058
$z : 15 - 25$ (SARAS 3)	0.064	0.078

**Table 3.** Median and mean errors in predicting power spectra given global signals over the REACH or SARAS 3 redshift bands. Here we consider simulated global signals without any added Gaussian random noise. These errors correspond to the histograms shown in Fig. 11.

### 5.2.4 Reconstruction of the 21-cm power spectrum using the SARAS 3 and REACH bands

In order to probe the effect of another typical observational constraint, we consider global signals limited to the redshift ranges of the REACH and SARAS 3 experiments. As before, we train a neural network, employ this trained network to reconstruct the 21-cm power spectrum, and then assess the prediction performance using equation 9. Here we consider the global signal without any added Gaussian noise. The analysis focuses on the same test models as discussed in Section 5.2, except that the global signals is limited to specific redshift bands. Several specific examples of comparison between the true and reconstructed 21-cm power spectra are presented in Figures D1 and D2 for the REACH and SARAS 3 redshift bands, respectively. To gauge the predictive capability for the power spectrum, we again quantify the errors using equation 9. The histogram of the errors is displayed in Figure 11, where the blue and dark orange histograms represent errors in the power spectrum reconstruction from global signals within the REACH and SARAS 3 redshift bands, respectively. The computed mean and median errors are presented in Table 3. The reconstruction error (both median and mean error) for the SARAS 3 band is larger by an approximate factor of 1.3 compared to that of the REACH band. Specifically, for power spectrum reconstruction utilizing global signals over the REACH redshift band, the median error is 0.050, while for the narrower SARAS 3 redshift band, this increases to 0.064.



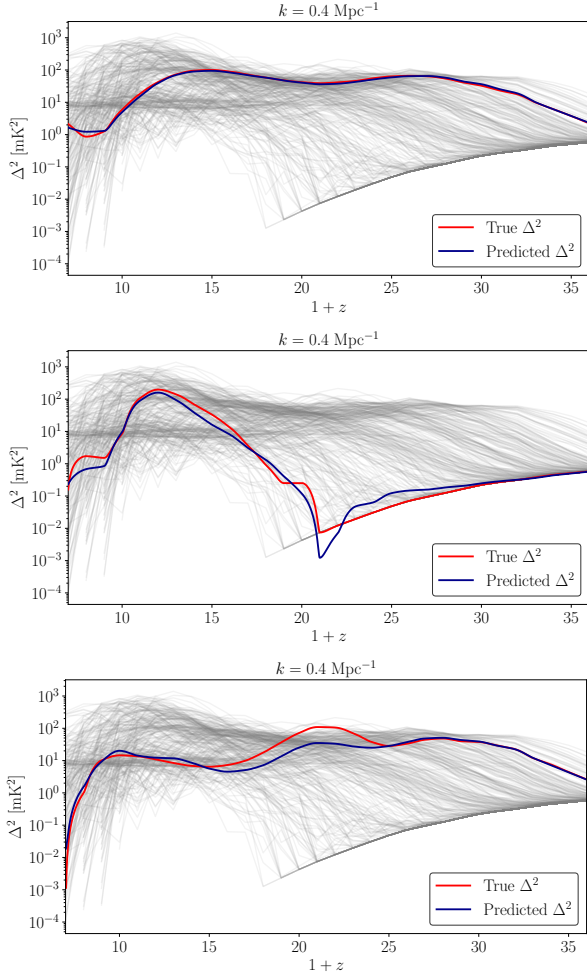


**Figure 10.** Comparison between the true power spectra from the simulation and the predicted power spectra from the trained network given the global signal. The level of error illustrated in each panel is as follows: Top panel: 10<sup>th</sup> percentile error (0.020), middle panel: median error (0.045), and bottom panel: 90<sup>th</sup> percentile error (0.092). We show the power spectra at  $k = 0.4 \text{ Mpc}^{-1}$  in all the panels. Here we use the models for the standard astrophysical scenario (CMB only). The gray lines in each panel represent all the samples in the test dataset.

## 6 CONCLUSIONS

We have studied the classification of various radio backgrounds using high-redshift 21-cm data. Typically, excess radio backgrounds are explored in the context of the EDGES low-band detection which requires extreme high-amplitude backgrounds. Here we focused on potentially more realistic cases, with moderate-amplitude radio backgrounds created by high-redshift galaxies. Such models are not usually considered but could be realized in nature. The motivation of this work was two-fold. First, we aimed to determine if an ANN classifier can pin down the nature of the radio background (here CMB-only, galaxies, or external). Secondly, we explored the possibility of utilizing an ANN to validate and verify if detected power spectra are consistent with global signal detections, once both are detected in the future. Here are some of our main findings.

(i) We built two ANN classifiers that can infer the type of radio background present at high redshifts given either the power spectrum or the global signal. These networks could be very useful as part of telescope inference pipelines by helping to identify and fit the most

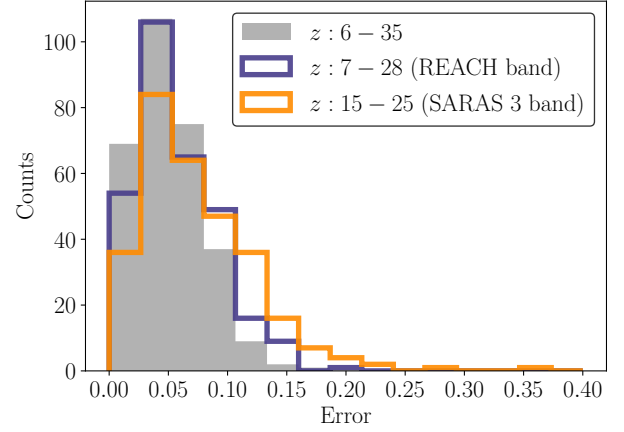


**Figure 11.** Same as Fig. 9, except that the power spectra are predicted based on the global signals over various redshift bands. Also, here we use the global signal samples without any added Gaussian random noise.

appropriate theoretical model to the observed data. We found that the network can predict the type of radio background with an overall accuracy of 96% based on a noiseless power spectrum and an overall accuracy of 90% based on a noiseless global signal given as input to the trained network. We show that models with an external radio background can be distinguished with an accuracy of 100% in these cases owing to the characteristic high-redshift behavior of this class of models. However, a significant fraction of galactic models are misclassified as having no radio excess. We next considered the case of signals contaminated by realistic observational effects. Using mock SKA power spectra results in a classification accuracy of 83% which is still reasonably good. Adding random Gaussian noise to the simulated global signal lowers the classification accuracy. However, with an optimistic sensitivity ( $\sim 2.5 \text{ mK}$ ) of next-generation global signal telescopes, the network can still infer the true standard astrophysical models and true external radio models with an accuracy of 94% and 93%, respectively. Going back to the noise-less case, we found that the accurate classification of the external radio background based on the global signal is consistent, regardless of the absorption amplitude. For observationally motivated limits on the redshift range, in the case of the broad REACH redshift band, the classifier can distinguish the external radio background effectively, achieving an accuracy above 90% for any depth of absorption deeper than 50 mK. Consequently, global signal observation through REACH-like experiments holds significant potential in discerning the presence or absence of an external radio excess in the 21-cm signal.

(ii) We constructed another ANN that can predict the global 21-cm signal over a wide range of redshifts given the 21-cm power spectrum. For the network where we used the power spectrum without any observational noise as the input, the error in the predicted global signal was 0.0094 (median), and less than 0.061 for 95% of test cases. Given the mock SKA 21-cm power spectrum calculated over the SKA  $z$  and  $k$ -bins, the network could still predict the global signal with a reasonably good accuracy, but with a significantly larger tail. The median error in this case was 0.035 but the 95% limit was much higher (0.33).

(iii) We designed an ANN to reconstruct the 21-cm power spectrum over a wide range of wavenumbers and redshifts given the global signal over the same redshift range. For standard astrophysical models, we found that the reconstruction error was 0.045 (median) and lower than 0.101 for 95% of the test models. For the models that as-

sume a category of excess radio background, the errors were similar, e.g., the 95<sup>th</sup> percentile error was 0.082 and 0.101 for external radio models and galactic radio models, respectively. These were the cases without any noise. We explored the effect of adding Gaussian noise at various levels, or limiting the global signal information over the REACH or SARAS 3 redshift band. While the errors increased, it remained possible to reconstruct the power spectrum with reasonable accuracy.

As it is still uncertain whether global signal experiments or radio interferometers will be able to robustly and accurately measure the 21-cm signal first, the trained network that can predict one signal from the other could play an important role of comparing the two approaches. Eventually, a demonstrated consistency between the results of the two approaches will go a long way towards convincing the broader astronomy community of the validity of the detections.

## ACKNOWLEDGEMENTS

SS and RB acknowledge the support of the Israel Science Foundation (grant No. 2359/20). AF is grateful for the support from the Royal Society through a University Research Fellowship.

This research made use of: Numpy (Harris et al. 2020), Scipy (Virtanen et al. 2020), matplotlib (Hunter 2007), Scikit-learn (Pedregosa et al. 2011) and the NASA Astrophysics Data System Bibliographic Services.

## DATA AVAILABILITY

The data underlying this article will be shared on reasonable request to the corresponding author.

## REFERENCES

- Abdurashidova Z., et al., 2022a, *ApJ*, 924, 51  
 Abdurashidova Z., et al., 2022b, *ApJ*, 925, 221  
 Acharya S. K., Cyr B., Chluba J., 2023, *MNRAS*, 523, 1908  
 Barkana R., 2018, *Nature*, 555, 71  
 Barkana R., Loeb A., 2004, *ApJ*, 609, 474  
 Barkana R., Outmezguine N. J., Redigol D., Volansky T., 2018a, *Phys. Rev. D*, 98, 103005  
 Barkana R., Outmezguine N. J., Redigol D., Volansky T., 2018b, *Phys. Rev. D*, 98, 103005  
 Barkana R., Fialkov A., Liu H., Outmezguine N. J., 2023, *Phys. Rev. D*, 108, 063503  
 Berlin A., Hooper D., Krnjaic G., McDermott S. D., 2018, *Phys. Rev. Lett.*, 121, 011102  
 Bevins H. T. J., Handley W. J., Fialkov A., de Lera Acedo E., Javid K., 2021, *MNRAS*, 508, 2923  
 Bevins H. T. J., Fialkov A., de Lera Acedo E., Handley W. J., Singh S., Subrahmanyan R., Barkana R., 2022, *Nature Astronomy*, 6, 1473  
 Bevins H. T. J., Heimersheim S., Abril-Cabezas I., Fialkov A., de Lera Acedo E., Handley W., Singh S., Barkana R., 2024, *MNRAS*, 527, 813  
 Biermann P. L., Nath B. B., Caramete L. I., Harms B. C., Stanev T., Becker Tjus J., 2014, *MNRAS*, 441, 1147  
 Bolgar F., Eames E., Hottier C., Semelin B., 2018, *MNRAS*, 478, 5564  
 Bowman J. D., Rogers A. E. E., Monsalve R. A., Mozdzen T. J., Mahesh N., 2018, *Nature*, 555, 67  
 Bye C. H., Portillo S. K. N., Fialkov A., 2022, *ApJ*, 930, 79  
 Cheung K., Kuo J.-L., Ng K.-W., Tsai Y.-L. S., 2019, *Physics Letters B*, 789, 137  
 Cohen A., Fialkov A., Barkana R., 2016, *MNRAS*, 459, L90  
 Cohen A., Fialkov A., Barkana R., Lotem M., 2017, *MNRAS*, 472, 1915  
 Cohen A., Fialkov A., Barkana R., Monsalve R. A., 2020, *MNRAS*, 495, 4845  
 Condon J. J., 1992, *ARA&A*, 30, 575  
 Cooray A., Li C., Melchiorri A., 2008, *Phys. Rev. D*, 77, 103506  
 Cyr B., Acharya S. K., Chluba J., 2024, *MNRAS*, 534, 738  
 Datta A., Bowman J. D., Carilli C. L., 2010, *The Astrophysical Journal*, 724, 526  
 DeBoer D. R., et al., 2017, *PASP*, 129, 045001  
 Dillon J. S., et al., 2014, *Physical Review D*, 89, 023002  
 Dowell J., Taylor G. B., 2018, *ApJ*, 858, L9  
 Eastwood M. W., et al., 2019, *AJ*, 158, 84  
 Ewall-Wice A., Chang T. C., Lazio J., Doré O., Seiffert M., Monsalve R. A., 2018, *ApJ*, 868, 63  
 Ewall-Wice A., Chang T.-C., Lazio T. J. W., 2020, *MNRAS*, 492, 6086  
 Feng C., Holder G., 2018, *ApJ*, 858, L17  
 Fialkov A., Barkana R., 2014, *MNRAS*, 445, 213  
 Fialkov A., Barkana R., 2019, *MNRAS*, 486, 1763  
 Fialkov A., Barkana R., Visbal E., Tseliakhovich D., Hirata C. M., 2013, *MNRAS*, 432, 2909  
 Fialkov A., Barkana R., Visbal E., 2014, *Nature*, 506, 197  
 Fialkov A., Cohen A., Barkana R., Silk J., 2017, *MNRAS*, 464, 3498  
 Fixsen D. J., et al., 2011, *ApJ*, 734, 5  
 Fragos T., et al., 2013, *ApJ*, 764, 41  
 Garsden H., et al., 2021, *MNRAS*, 506, 5802  
 Gehlot B. K., et al., 2019, *MNRAS*, 488, 4271  
 Gilfanov M., Grimm H. J., Sunyaev R., 2004, *MNRAS*, 347, L57  
 Greig B., Mesinger A., 2015, *MNRAS*, 449, 4246  
 Grimm H. J., Gilfanov M., Sunyaev R., 2003, *MNRAS*, 339, 793  
 Gürkan G., et al., 2018, *MNRAS*, 475, 3010  
 HERA Collaboration et al., 2023, *ApJ*, 945, 124  
 Haiman Z., Rees M. J., Loeb A., 1997, *ApJ*, 476, 458  
 Han J., Moraga C., 1995, in International Work-Conference on Artificial and Natural Neural Networks. <https://api.semanticscholar.org/CorpusID:2828079>  
 Harris C. R., et al., 2020, *Nature*, 585, 357  
 Hunter J. D., 2007, *Computing in Science & Engineering*, 9, 90  
 Jana R., Nath B. B., Biermann P. L., 2019, *MNRAS*, 483, 5329  
 Jensen H., Majumdar S., Mellema G., Lidz A., Iliev I. T., Dixon K. L., 2015, *Monthly Notices of the Royal Astronomical Society*, 456, 66  
 Jolliffe I. T., Cadima J., 2016, *Philosophical Transactions of the Royal Society of London Series A*, 374, 20150202  
 Kern N. S., Liu A., Parsons A. R., Mesinger A., Greig B., 2017, *ApJ*, 848, 23  
 Kingma D. P., Ba J., 2014, *arXiv e-prints*, p. arXiv:1412.6980  
 Koopmans L., et al., 2015, in Advancing Astrophysics with the Square Kilometre Array (AASKA14). p. 1 (arXiv:1505.07568)  
 Kovetz E. D., Poulin V., Gluscevic V., Boddy K. K., Barkana R., Kamionkowski M., 2018, *Phys. Rev. D*, 98, 103529  
 Levin D. A., Peres Y., Wilmer E. L., 2006, Markov chains and mixing times. American Mathematical Society, [http://scholar.google.com/scholar.bib?q=info:3wf9IU94tyMJ:scholar.google.com/&output=citation&hl=en&as\\_sdt=2000&ct=citation&cd=0](http://scholar.google.com/scholar.bib?q=info:3wf9IU94tyMJ:scholar.google.com/&output=citation&hl=en&as_sdt=2000&ct=citation&cd=0)  
 Lewis A., 2011, *J. Cosmology Astropart. Phys.*, 2011, 026  
 Lewis A., Challinor A., Lasenby A., 2000, *ApJ*, 538, 473  
 Liu H., Outmezguine N. J., Redigolo D., Volansky T., 2019, *Phys. Rev. D*, 100, 123011  
 Majumdar S., Pritchard J. R., Mondal R., Watkinson C. A., Bharadwaj S., Mellema G., 2018, *MNRAS*, 476, 4007  
 Mertens F., Semelin B., Koopmans L., 2021, arXiv preprint arXiv:2109.10055  
 Mesinger A., Furlanetto S., Cen R., 2011, *Monthly Notices of the Royal Astronomical Society*, 411, 955  
 Mineo S., Gilfanov M., Sunyaev R., 2012, *MNRAS*, 419, 2095  
 Mirocha J., Furlanetto S. R., 2019, *MNRAS*, 483, 1980  
 Mondal R., et al., 2020, *MNRAS*, 498, 4178  
 Monsalve R. A., et al., 2024, *MNRAS*, 530, 4125  
 Muñoz J. B., Loeb A., 2018, arXiv e-prints, p. arXiv:1802.10094  
 Nair V., Hinton G. E., 2010, in Proceedings of the 27th international conference on machine learning (ICML-10). pp 807–814

- Pacucci F., Mesinger A., Mineo S., Ferrara A., 2014, *MNRAS*, 443, 678
- Pedregosa F., et al., 2011, *Journal of Machine Learning Research*, 12, 2825
- Philip L., et al., 2019, *Journal of Astronomical Instrumentation*, 8, 1950004
- Planck Collaboration et al., 2020, *A&A*, 641, A6
- Pober J. C., 2015, *Monthly Notices of the Royal Astronomical Society*, 447, 1705
- Pober J. C., et al., 2014, *The Astrophysical Journal*, 782, 66
- Press W. H., Schechter P., 1974, *ApJ*, 187, 425
- Price D. C., et al., 2018, *MNRAS*, 478, 4193
- Ramchoun H., Idrissi M. A. J., Ghanou Y., Ettaouil M., 2016, *Int. J. Interact. Multim. Artif. Intell.*, 4, 26
- Rees M. J., 1986, *MNRAS*, 222, 27P
- Reis I., Fialkov A., Barkana R., 2020, *MNRAS*, 499, 5993
- Reis I., Fialkov A., Barkana R., 2021, *MNRAS*, 506, 5479
- Reis I., Barkana R., Fialkov A., 2022, *ApJ*, 933, 51
- Rumelhart D. E., Hinton G. E., Williams R. J., 1986, *Nature*, 323, 533
- Schmit C. J., Pritchard J. R., 2018, *MNRAS*, 475, 1213
- Seiffert M., et al., 2011, *ApJ*, 734, 6
- Sheth R. K., Tormen G., 1999, *MNRAS*, 308, 119
- Sikder S., Barkana R., Reis I., Fialkov A., 2024a, *MNRAS*, 527, 9977
- Sikder S., Barkana R., Fialkov A., Reis I., 2024b, *MNRAS*, 527, 10975
- Singh S., et al., 2022, *Nature Astronomy*, 6, 607
- Sobacchi E., Mesinger A., 2013, *MNRAS*, 432, 3340
- Songaila A., Cowie L. L., 2010, *ApJ*, 721, 1448
- Trott C. M., et al., 2020, *MNRAS*, 493, 4711
- Tselikhovich D., Hirata C., 2010, *Phys. Rev. D*, 82, 083520
- Urry C. M., Padovani P., 1995, *PASP*, 107, 803
- Virtanen P., et al., 2020, *Nature Methods*, 17, 261
- Visbal E., Barkana R., Fialkov A., Tselikhovich D., Hirata C. M., 2012, *Nature*, 487, 70
- Voytek T. C., Natarajan A., Jáuregui García J. M., Peterson J. B., López-Cruz O., 2014, *ApJ*, 782, L9
- Wyithe J. S. B., Loeb A., 2004, *Nature*, 432, 194
- de Lera Acedo E., et al., 2022, *Nature Astronomy*,

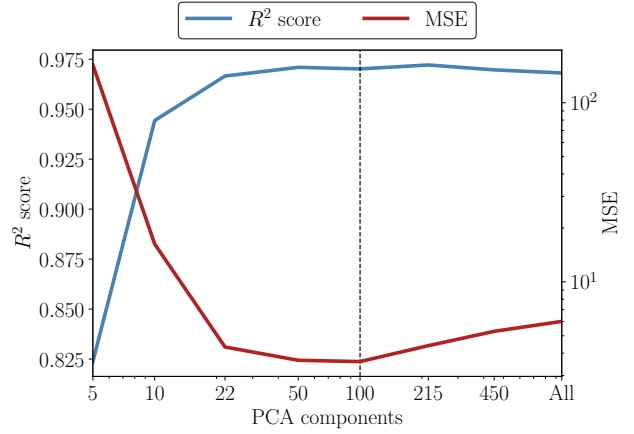


**Figure A1.** The impact of dimensionality reduction of the power spectrum dataset in the context of predicting the global signal given the power spectrum spectrum without any observational effects. We show how the two regression performance estimators,  $R^2$  score and MSE, vary with the number of PCA components in the learning model. The dashed vertical line shows the optimum number of components.

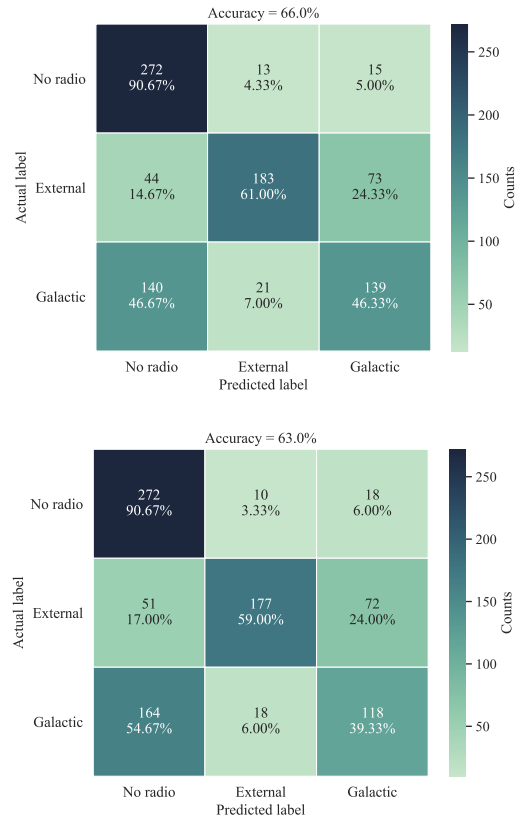


**Figure B1.** The performance of the classification procedure using the global signal with added Gaussian noise. The top panel is for Gaussian noise of  $\sigma = 17$  mK, and the bottom panel for  $\sigma = 25$  mK.

## APPENDIX A: SELECTING THE OPTIMAL PCA COMPONENTS FOR THE NETWORK PREDICTING THE GLOBAL SIGNAL

In order to set an appropriate number of principal components in section 5.1.1 we use two utility functions that measure regression performance:  $R^2$  score and mean squared error (MSE). We show an example in Fig. A1 of how these two functions vary with the number of PCA components. We select the optimum number of components where the  $R^2$  score is maximized and the MSE minimized.

## APPENDIX B: PERFORMANCE OF THE CLASSIFICATION IN THE CASE OF A NOISY GLOBAL SIGNAL

When considering classification in section 5.1.1, in order to study the network's ability to infer the radio background in more practical situations, two more noisy global 21-cm datasets were used. Random Gaussian noise was added to the simulated global 21-cm signal in order to consider the effect of the typical uncertainty of existing global signal telescopes on the classification procedure. Adding Gaussian noise with  $\mu = 0$  and  $\sigma = 17$  mK or 25 mK (top and bottom panel of Fig. B1, respectively) results in an overall classification accuracy of 64% and 61%, respectively.

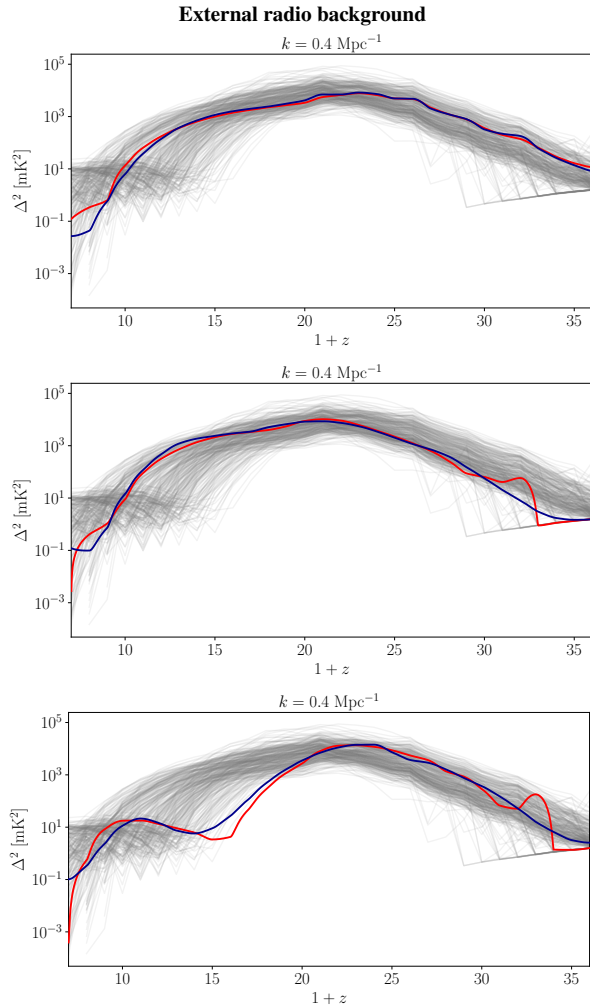


**Figure C1.** Comparison between the true and predicted 21-cm power spectra with an external radio background. The error level for each panel is as follows: Top panel: 10<sup>th</sup> percentile error (0.022), middle panel: median error (0.044), and bottom panel: 90<sup>th</sup> percentile error (0.072). We show the power spectrum at  $k = 0.4 \text{ Mpc}^{-1}$  in all the panels. Shown here is the case without any observational noise.

#### APPENDIX C: EXAMPLES OF COMPARISON BETWEEN THE PREDICTED AND TRUE 21-CM POWER SPECTRUM WITH AN EXCESS RADIO BACKGROUND

In section 5.2.2 we considered the reconstruction of the 21-cm power spectrum given the global 21-cm signal. To show the quality of reconstructions of 21-cm power spectra in the case of excess radio models, the comparison between true and predicted power spectra is shown in Fig. C1 for an external radio background, and in Fig. C2 for the case of a galactic radio background, for a few specific models. Here we use excess radio models without any observational effects.

#### APPENDIX D: EXAMPLES OF COMPARISON BETWEEN THE PREDICTED AND TRUE 21-CM POWER SPECTRUM FROM THE GLOBAL SIGNAL OVER THE REACH OR SARAS 3 BAND

In section 5.2.4 we considered the reconstruction of the 21-cm power spectrum given the global 21-cm signal. In order to evaluate the

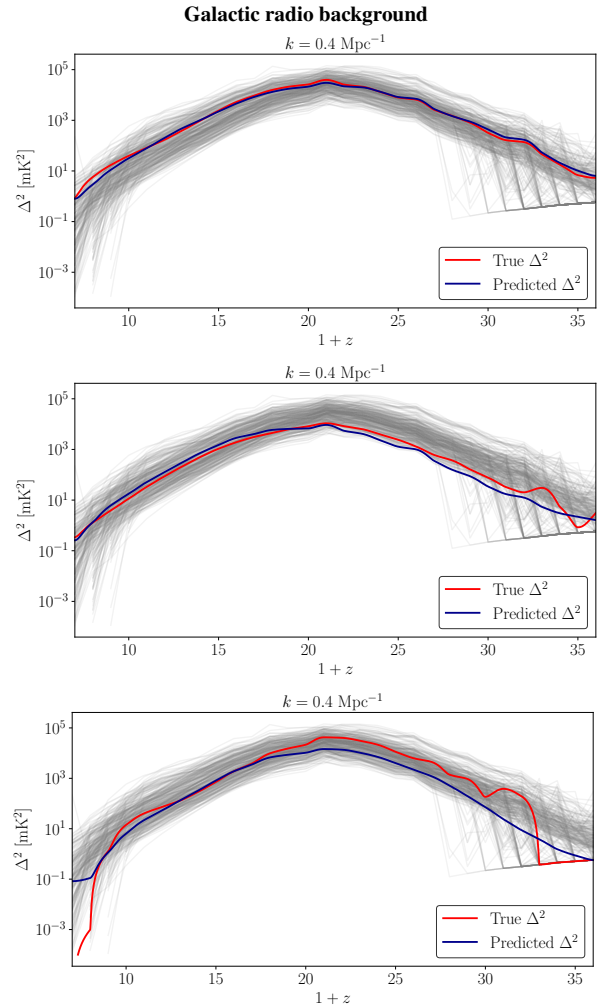


**Figure C2.** Comparison between the true and predicted 21-cm power spectra with a galactic radio background. The error level for each panel is as follows: Top panel: 10<sup>th</sup> percentile error (0.041), middle panel: median error (0.058), and bottom panel: 90<sup>th</sup> percentile error (0.094). We show the power spectrum at  $k = 0.4 \text{ Mpc}^{-1}$  in all the panels. Shown here is the case without any observational noise.

quality of the power spectrum prediction model from a global signal over redshift ranges accessible to experiments such as REACH and SARAS 3, we present a few specific model comparisons in Fig. D1 and D2. Here we used the global signal without added Gaussian random noise.

This paper has been typeset from a  $\text{\TeX}/\text{\LaTeX}$  file prepared by the author.



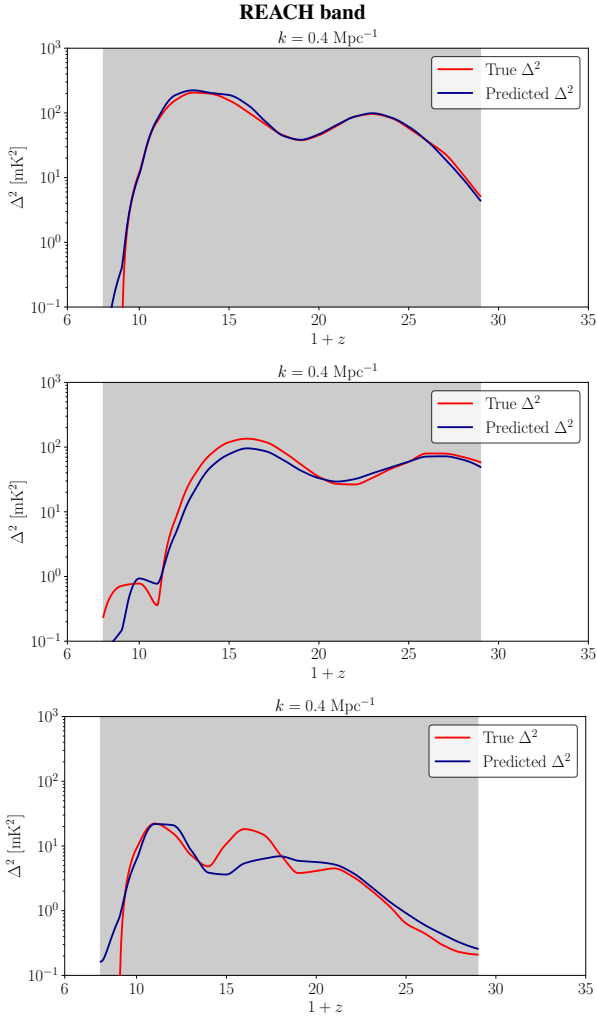


**Figure D1.** Comparison between the true and predicted 21-cm power spectra for standard astrophysical models using the REACH redshift band. The error level for each panel is as follows: Top panel: 10'th percentile error (0.022), middle panel: median error (0.050), and bottom panel: 90'th percentile error (0.103). We show the power spectrum at  $k = 0.4 \text{ Mpc}^{-1}$  in all the panels. Shown here is the case without any observational noise.

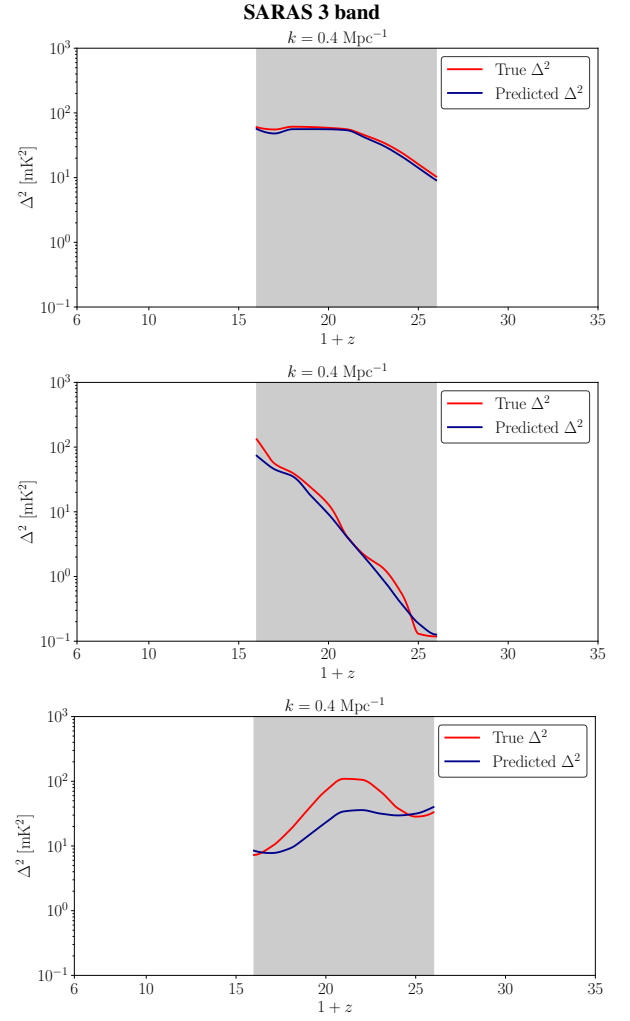


**Figure D2.** Comparison between the true and predicted 21-cm power spectra for standard astrophysical models using the SARAS 3 redshift band. The error level for each panel is as follows: Top panel: 10'th percentile error (0.025), middle panel: median error (0.064), and bottom panel: 90'th percentile error (0.134). We show the power spectrum at  $k = 0.4 \text{ Mpc}^{-1}$  in all the panels. Shown here is the case without any observational noise.